

Submitted to *The Astrophysical Journal Supplement*

# Toward High Precision Seismic Studies of White Dwarf Stars: Parametrization of the Core and Tests of Accuracy

N. Giammichele<sup>1,2,3</sup>, S. Charpinet<sup>2,3</sup>, G. Fontaine<sup>1</sup>, and P. Brassard<sup>1</sup>

## ABSTRACT

We present a prescription for parametrizing the chemical profile in the core of white dwarfs in the light of the recent discovery that pulsation modes may sometimes be deeply confined in some cool pulsating white dwarfs. Such modes may be used as unique probes of the complicated chemical stratification that results from several processes that occurred in previous evolutionary phases of intermediate-mass stars. This effort is part of our ongoing quest for more credible and realistic seismic models of white dwarfs using static, parametrized equilibrium structures. Inspired from successful techniques developed in design optimization fields (such as aerodynamics), we exploit Akima splines for the tracing of the chemical profile of oxygen (carbon) in the core of a white dwarf model. A series of tests are then presented to better seize the precision and significance of the results that can be obtained in an asteroseismological context. We also show that the new parametrization passes an essential basic test, as it successfully reproduces the chemical stratification of a full evolutionary model.

*Subject headings:* stars: oscillations — stars : interiors — chemical stratification — white dwarfs

## 1. INTRODUCTION

In the era of space missions such as *Kepler* and *Kepler-2* (K2) which have been providing asteroseismic data of unprecedented quality for several types of pulsating stars (including

---

<sup>1</sup>Département de Physique, Université de Montréal, Montréal, QC H3C 3J7, Canada

<sup>2</sup>Université de Toulouse, UPS-OMP, IRAP, Toulouse F-31400, France

<sup>3</sup>CNRS, IRAP, 14 avenue Edouard Belin, F-31400 Toulouse, France

white dwarfs), we decided to revisit the problem of the seismic modeling of this latter type of pulsators using current techniques, typical of those developed quite successfully in recent years for pulsating hot B subdwarfs (see, e.g., Charpinet et al. 2013). To test these techniques in a white dwarf context, we first carried out a detailed analysis of the pulsation properties of two classical hot ZZ Ceti stars – GD 165 and Ross 548 – using the best available data from the ground. Those targets were chosen on the basis of the simplicity of their light curves (associated with their locations near the blue edge of the ZZ Ceti instability strip), their near spectroscopic twin nature, and the availability of time-series data sets of exceptional quality. The results of that analysis were presented by Giammichele et al. (2015; 2016) who found a credible seismic model for each star able to reproduce simultaneously the six observed periods well within  $\sim 0.3\%$  on the average, which is comparable to the best results achieved so far in asteroseismology. The models provided robust mode identification and were found to be perfectly compatible with the expectations of linear pulsation theory in both its adiabatic and nonadiabatic versions. In addition, these seismic models were shown to be consistent with all the available external independent constraints such as estimates of the atmospheric parameters derived from time-averaged spectroscopy, estimates of distances provided by parallax measurements or spectroscopy, and even the measured rate of period change for one mode in Ross 548. The study of Giammichele et al. (2015; 2016) thus firmly established that our approach to quantitative seismology – based on static, parametrized models of stars – can be extended reliably to the white dwarf domain.

An unexpected result of the study of Giammichele et al. (2016) is the finding that the pulsation periods detected in GD 165 bear only a weak dependence on the core composition, while those observed in Ross 548 are, on the contrary, quite sensitive to a variation of the core composition. This a priori puzzling result finds a natural explanation in that all six modes in the GD 165 model have amplitudes and weight functions that do not extend into the deep core and, consequently, their periods are not sensitive to a variation of the core composition. In comparison, three of the six modes of interest in the Ross 548 model are partly confined below its thin envelope and, therefore, bear a strong sensitivity on the core composition. This discovery of the existence of deeply confined modes in Ross 548 and, potentially, in many other pulsating white dwarfs, opens up the most interesting possibility of using those modes as probes of the internal composition profile in the C-O core. In the Giammichele et al. (2016) study, to keep things as simple as possible, it was assumed that the core composition is homogeneous, which is a crude approximation in the light of the rather complicated C-O stratification expected in the cores of former AGB stars as revealed by detailed evolutionary calculations (see, e.g., Salaris et al. 2010 or Romero et al. 2012). In retrospect, such an approximation was amply sufficient in the case of GD 165, but it is now clear that for stars such as Ross 548, with deeply confined modes, our modeling

could be perfected by including a parametrized description of the chemical layering in the C-O core. Presumably, this would lead to still more realistic seismic models of pulsating white dwarfs, with theoretical periods approaching the “Holy Grail” of asteroseismology, i.e., perhaps able to reproduce the observed periods at the accuracy of the observations. Currently, as indicated above, the best one can do is to obtain average dispersions of less than  $\sim 0.3\%$  in periods, still a long way from the measurement uncertainties as indicated, for example, in Tables 3 and 4 of Giammichele et al. (2015). The advent of ultra-high precision photometry from space, in particular with the *Kepler* mission, further enlarges this gap as some pulsation frequencies can be measured with outstanding precision of the order of nanohertz. Six pulsating white dwarfs were extensively monitored with *Kepler* (see, e.g., Østensen et al. 2011; Greiss et al. 2014, 2015) and high precision data for more objects have been (or will be) delivered by the still ongoing K2 mission (Hermes et al. 2014; Howell et al. 2014). Thus, there are exceptionally high-quality data available for a handful of pulsating white dwarfs that should provide particularly stringent testbeds for asteroseismology. We present, in this paper, a prescription for parametrizing the C-O core of a white dwarf, with the hope of improving future seismic models of stars of this type. We also discuss series of tests that evaluate the precision that can potentially be achieved on stellar and structural parameters with our technique.

## 2. PARAMETRIZATION OF THE CORE OF A WHITE DWARF

### 2.1. The Need for a New Parametrization

Parametrizing the core composition is not by itself a new idea as several attempts have been made in the past to improve white dwarf modeling for the purposes of asteroseismic studies. Different parametrizations for the distribution of chemical species in the core were employed, the simplest one being a fixed homogeneous core. For instance, Brassard et al. (1992) explored the potential of white dwarf seismology, with the study of the adiabatic properties of pulsating DA white dwarfs, by using a homogeneous carbon core in their calculations (see also Fontaine & Brassard 2002). More recently, Castanheira & Kepler (2008; 2009) also used a fixed homogeneous C/O core (50% each in mass fraction) through their analyses of 83 ZZ Ceti stars. The main argument that was used to justify this crude approach was simplicity, in view of the usual paucity of observed periods and the perceived need to limit the number of free parameters that would characterize a model. In addition, on general grounds, it was expected that the g-modes detected in the more evolved, more degenerate pulsating white dwarfs, the ZZ Ceti stars in particular, would not be very sensitive to the details of the core structure because of the outward migration of g-mode amplitudes and weight

functions associated with the cooling process. This can indeed be true when the detected modes do not propagate deep inside the star, but this is not the case in presence of modes confined below the helium mantle as discussed by Giammichele et al. (2016). This simple parametrization has also the benefit of not requiring the use of any additional parameter in the search for a best-fit solution to the observed pulsation periods. Nevertheless, it remains very far from even approaching expected chemical profiles evolved from the zero age main sequence (ZAMS), according to calculations from different groups over the years (e.g., Salaris et al 1997, Althaus et al. 2002, and Straniero et al. 2003, just to mention a few). According to these evolutionary calculations, the oxygen profile inside the core of a white dwarf follows a rather complicated descent from an inner central homogeneous part, while carbon is the complementary element to it in that region. Moreover, it is found that the point where the mass fraction of oxygen is about to vanish is located above an interface where three elements, carbon, oxygen and helium, can coexist in roughly comparable proportions.

A first step in dealing more rigorously with core C/O profiles in models of white dwarfs built for asteroseismology was performed by Bradley (1996) who used a ramp-like shape as described by Wood (1992), i.e., a simplified version of the oxygen-rich core profiles computed by Mazzitelli & D’Antona (1986a; 1986b). The core of this model is set to a homogeneous central part with 80 % (in mass) of oxygen out to  $0.75 M_*$  and it linearly changes to pure carbon by  $0.90 M_*$ . The central mass fraction of oxygen and the location of the C/O transition zone has been allowed to vary for a few possible configurations in the study of mode trapping in ZZ Ceti stars in Bradley (1996), as well as in the study of the two pulsators G117-B15A and Ross 548 (Bradley 1998), and later in a similar exercise concerning L19-2 and GD 165 (Bradley 2001). However, a major caveat of the optimization technique performed at the time was the non-simultaneous fitting of the various parameters and the use of a coarse grid of models as imposed by the evolutionary approach. Even if the descent in the transition zone turns out to be more realistic when compared to a basic homogeneous core, this approach remains relatively crude. In particular, the triple transition of carbon, oxygen and helium is still not a possible configuration of this parametrization, as the limit of  $0.90 M_*$  where the pure carbon layer exists is fixed, and the helium mantle is too thin to be connected to the oxygen reservoir. Moreover, the oxygen descent is not closely reproduced when compared to what is found from detailed evolutionary models with a ZAMS connection.

A more sophisticated core treatment came from Metcalfe (2005) who introduced for the first time a parametrization that tries to mimic the features of an evolutionary-based chemical profile for the C-O white dwarf core, using Salaris et al. (1997) evolutionary tracks. This parametrization employs two free parameters defining the constant central abundance of oxygen,  $X(\text{O})$ , and the fractional mass,  $q$ , at which the constant oxygen mass fraction starts dropping. The shape of the drop is simply taken to be a scaled version of an evolutionary

track from the work of Salaris et al. (1997) at the specific white dwarf mass of  $M_* = 0.61 M_\odot$ . Moreover, the drop ends at the fixed value of  $0.95 M_*$ . While doing a better job in reproducing a specific core composition profile than the other proposed recipes (relative to what is expected from stellar evolution calculations), these physically motivated C/O profiles suffer from a major lack of flexibility. The pre-determined parameters and shape do not allow a thorough search in the stellar model space (there are only few configurations possible with two parameters) and this lack of flexibility does not allow a proper testing of the core chemical profiles. Quite notably, this parametrization fails at simply reproducing the core composition profiles from detailed evolutionary models at other masses. They also fail, like other methods discussed before, at reproducing the triple chemical transition at the edge of the core, where oxygen, carbon, and helium are expected to coexist, according to current evolutionary sequences computed to produce white dwarfs star (see, e.g., Althaus et al. 2010). Here again, this is an important limitation as the pulsations properties can be influenced by those major predicted features.

For completeness, we also mention the efforts developed these past ten years to tackle asteroseismology of white dwarf stars from a different angle by using evolutionary models computed from the ZAMS (e.g., Romero et al. 2012), or parametrized white dwarf evolutionary models with pre-computed C/O profiles from grids of evolutionary models from the ZAMS (e.g., Chen 2016). However, this approach, by definition, leaves no flexibility at all at the level of the core structure and does not constitute an option for our purposes, i.e., testing white dwarf stellar structure with asteroseismology and, in particular, the predictions of stellar evolution calculations. For this, we need an independent tool, a new method to model and parametrize the core composition that does not incorporate parts of pre-calculated profiles. We need a tool that is capable of reproducing closely enough the stratification obtained in evolutionary models, but which at the same time leaves open the possibility that the composition profiles in the core of real white dwarfs may be different from what is currently predicted. Relying heavily on pre-calculated profiles would clearly not allow such tests.

In this context, we are thus left with a need for a new parametrization for the core composition which would be more robust and flexible than previous recipes proposed so far. We also need this new parametrization to be coupled with our modern tools for asteroseismology based on a set of powerful optimizations codes (see, e.g., the Introduction of Giammichele et al. 2016, or Charpinet et al. 2015 and references therein). We describe in the following subsection how these developments are implemented.

## 2.2. Implementation of the New Parametrization

In our seismic studies, the problem revolves around minimizing a merit function defined by the sum of the squared differences between theoretical and observed periods obtained for a specific star (see, e.g., Giammichele et al. 2016). In our previous efforts on GD 165 and Ross 548, we fixed the convective efficiency to a standard version, we also imposed fixed composition profiles at the H-He and He-core interfaces as obtained from detailed evolutionary calculations of GD 165 taking into account diffusion between the atomic species. We were thus left with five parameters to define a full, static model of a ZZ Ceti star : (1) the surface gravity, (2) the effective temperature, (3) the mass contained in the He mantle, (4) the mass contained in the H outermost layer, and (5) the core composition. Given the small number of modes available (six for both GD 165 and Ross 548), we strove to keep the number of free parameters to a minimum value, so we assumed crudely that the composition in the core would be homogeneous and specified by a single quantity, the oxygen mass fraction  $X(\text{O})$ . We now consider a more realistic depth-dependent core composition as obtained from detailed evolutionary calculations.

Inferring the most realistic composition profile given an ensemble of observed periods sensitive to the details of the core can be defined as a shape optimization problem. As generally stated, shape optimization, or optimal design, is the set of methods that gives the best possible form in order to fulfill the desired requirements. The typical problem is to find the shape which is optimal in that it minimizes a certain cost, or merit, function while satisfying given constraints. These methods are widely encountered in various domains such as aerodynamics, hydrodynamics, acoustics, electromagnetism, and many more. Our situation, the “drawing” of the chemical profile to best match what is occurring in stars, quantified by the minimization of our merit function, is, in all particulars, analogous to airfoil shape optimization, just to name one.

In general, the ideal airfoil shape, entirely defined by a set of parameters, is determined by minimizing a simple merit function. In the case of aerodynamic problems, the merit function to minimize is usually defined to be the inverse of the lift-to-drag ratio. It is important to realize that the number of parameters used to define the airfoil shape has nothing to do with the number of quantities involved in the merit function. Every single airfoil shape give a lift-to-drag ratio, independently of the number of parameters that are needed to define the shape of the airfoil. We adopt the exact same approach for parametrizing the chemical profile of the core. Every single shape of the chemical profile leads to a single merit function value, independent of the adopted parametrization of the shape and no matter how many periods (that enter into the merit value computation) are observed.

If the parametrization technique is not flexible enough, which translates into not being



able to represent all possible shapes, then a true optimal shape cannot generally be attained. On the other hand, if the number of design parameters is too large, the optimization problem becomes unfeasible in term of excessive computational time. Different shape parametrizations have been used in the aerodynamic field, among others: analytical, discrete, polynomial and spline representations (Gallart 2002). Every method has its advantages and drawbacks. In the analytic representation, given an original shape, a set of functions deform that shape. The design variables control the deformations added to the original shape in order to create the new shape. This method has the advantage of reducing the necessary number of design variables to a small set, while obtaining a smooth surface. On the other hand, it is only applicable to simple geometries and the deformations are dependent on the shape functions used. The discrete representation is more flexible, easy to implement, and can be used with any geometry. However, it requires a large number of design variables and the final shape can have high frequency oscillations. With polynomial methods, the design variables are the coefficients of a polynomial. The main advantage in this method is that a small set of design variables can be used, but as for analytical methods, if only low order polynomials are considered, some shapes become impossible to represent. The most commonly used representations in areas of expertise such as aerodynamics or automobile design are the spline representations, being the sum of weighted polynomials. In this case, the set of weighting parameters, called control points, are used as the design variables. There exist several types of splines: Bezier curves, B-splines and non-uniform rational B-spline (NURBS), just to name a few. There are several reasons for using splines: it allows for a reduction in the number of control points (or design variables); the perturbation of one control point has only local effects on the design shape; it produces curves with  $C^2$  continuity, therefore guaranteeing a shape that is smooth enough without high frequency oscillations.

In our context, we adopt spline representations to reproduce the oxygen chemical profile in a white dwarf core. The left panel of Figure 1 introduces the different design parameters that constitute the new parametrization. These parameters define a set of control points through which interpolation is done (right panel of the same figure). After testing various options, we opt for an interpolation scheme using Akima splines (Akima 1970). The Akima interpolation is a continuously differentiable sub-spline interpolation. It is built from piecewise third order polynomials. Only data from the next neighbor points is used to determine the coefficients of the interpolation polynomial. The disadvantage of other schemes, such as cubic splines, is that they can oscillate in the neighborhood of an outlier or when gradients change abruptly (as illustrated in Figure 1). This is also known as “Gibbs noise”. The Akima spline is a special spline which is stable against such points and provides a robust and smooth representation of the chemical stratification in the core. The shape parameters that control the Akima splines are specifically chosen in order to best imitate the main structures

in an evolved white dwarf chemical profile (see, again, Salaris et al. 2010 or Romero et al. 2012). Eight design parameters are necessary to fully define a two-transition chemical profile in the core: core O,  $t1$ ,  $\Delta t1$ ,  $t1(O)$ ,  $t2$ ,  $\Delta t2$ ,  $t2(O)$ , and envl O. We point out that the last parameter, envl O, is here to account for specific configurations involving DB white dwarfs for which it is believed that the oxygen mass fraction does not drop to zero at the edge of the C/O core. In a DA white dwarf context, which will be the main focus in this paper, the envl O parameter is always set to zero and the problem technically reduces to a seven parameter shape optimization. The proposed parametrization is flexible enough that it allows us to define a simpler one-transition profile by only using a subset of three shape parameters, core O,  $t1$  and  $\Delta t1$ . In that case and by construction, in order to have a smooth profile,  $t1(O)$  and  $t2(O)$  are set to zero, while the value of  $t2$  is set far enough not to interfere and  $\Delta t2$  is given a non-zero value.

The main improvement of this new parametrization relies on the definition of the oxygen profile as just described. The rest of the structure is defined using our standard procedure for building static parametrized models as described in Giammichele et al. (2016). For the benefit of the reader, however, we briefly recall here the approach that we have adopted for parametrizing the envelope as well. We address the definition of the envelope by using four different parameters:  $D(H)$ ,  $D(He)$ ,  $Pf_H$ , and  $Pf_{He}$ . In order to specify the quantity of hydrogen and helium in the star, the two parameters  $D(H)$  and  $D(He)$  are necessary and are directly proportional to the total (logarithmic) mass fraction of hydrogen and helium.  $D(H)$  and  $D(He)$  indicate the middle of the H/He and He/C/O transitions, respectively. The shape of the transition at the border of the H/He and the He/C/O layers is based on equations (26) and (28) of Tassoul et al. (1990) that define the profile for the tail of the complementary trace element when diffusive equilibrium is assumed. The two parameters  $Pf_H$  and  $Pf_{He}$  are introduced to be scaling factors that allow to compensate for the potentially unreached diffusive equilibrium and allow to explore a large range of possible shapes from sharp to broad. The implicit equation governing the chemical profile of two species in a transition zone is given by:

$$\frac{X_2^{A_1}}{X_1^{A_2}} \left( \frac{A_1 X_2 + A_2 X_1}{A_1 + A_2} \right)^{A_2 - A_1} = \left( \frac{q}{D} \right)^{P_f [A_2(Z_1+1) - A_1(Z_2+1)]}, \quad (1)$$

where  $A_i(Z_i)$  corresponds to the atomic weight (average charge evaluated at the middle of the transition zone) of element  $i$ ,  $D$  is the value of  $q$  where  $X_1 = X_2 = 0.5$  and  $P_f$  is the scaling factor (1 when diffusive equilibrium is reached). Such a functional form belongs to the so-called family of sigmoid functions. In the case where three elements overlap, such as the extension of the He tail into the outer regions of the C/O core for example, we still use the above equation with element 1 representing He, but “element 2” being the weighted sum of the contributions of C and O to the local values of  $X_2$ ,  $A_2$ , and  $Z_2$ . Of course, in the



innermost part of the core where  $X(\text{He})$  and  $X(\text{H})$  fall to zero, the carbon mass fraction is simply given by  $X(\text{C}) = 1 - X(\text{O})$ .

Figure 2 presents a comparison of three helium profiles culled from a representative DA evolutionary sequence incorporating diffusion (the solid black curves) with the results of our fitting procedure obtained by varying the four envelope parameters (the red dotted curves), in particular  $Pf_{\text{H}}$  and  $Pf_{\text{He}}$ . Our computed evolutionary sequence is characterized by a total mass of  $M_* = 0.6 M_{\odot}$  and an envelope layering specified by  $\log M(\text{He})/M_* = -3.0$  and  $\log M(\text{H})/M_* = -5.0$ . We can observe that the overall shape and, specifically, the asymmetry in the evolving profile of helium is well matched by the parametrized chemical profile in both the case of the H/He transition and of the He/C/O transition. Note that in the rest of this paper the argumentation is focussed on the parametrization of the core, not the envelope. Consequently, for the sake of simplicity and for the unique purpose of this paper,  $Pf_{\text{H}}$  and  $Pf_{\text{He}}$  were not varied and left to their calibrated values obtained from evolutionary calculations performed for the pulsating white dwarf star GD 165, as mentioned in Giammichele et al. (2016).

With the above prescription, we now have in hands a new parametrization that can imitate smoothly enough one or two steep ”drops” in the oxygen profile (and complementarily the carbon profile) in the core, without directly relying on a specific evolutionary model. Quite importantly, the flexibility of this parametrization also allows, as one of its many configurations, the triple transition at the edge of a rather thick helium mantle, between helium, carbon and oxygen, as predicted by evolutionary calculations. This triple transition was never a possibility in previous works using parametrized models, as mentioned in details in the previous subsection. Figure 3 indeed illustrates how well this new parametrization can mimic generic profiles obtained from evolutionary calculations for a typical DA white dwarf (left panel) adjusted to match the model shown in Althaus et al. (2010) (their Figure 6), and for a typical DB white dwarf (right panel) adjusted to match the evolutionary model presented in Córscico et al. (2012) (their Figure 2).

In the following section, we validate this new parametrization through a series of tests more generally aimed at evaluating the theoretical precision that can be achieved with white dwarf asteroseismology in various contexts.

### 3. TESTS ON THE PRECISION ACHIEVABLE WITH ASTEROSEISMOLOGY

The measurements of white dwarf stellar parameters using asteroseismology are quite precise by current standards, if we refer to the latest analysis of Ross 548 and GD 165 as alluded to above. However, periods are still not fitted at the precision of the observations, indicating that uncertainties are dominated by shortcomings in the models and suggesting that the potential of this technique is not yet fully exploited. In this section, we are interested in testing the degree of precision we can expect on the measured stellar parameters from the results of a seismic analysis if the uncertainties were only coming from observations, either ground- or space-based.

To test this, we start by creating an artificial reference star from a pulsating white dwarf model with given global and structural (shape) parameters. The structure and pulsation properties of this reference star are thus entirely known. We then select a subset of 10  $\ell = 1$  and 2  $g$ -modes out of the pulsation spectrum to simulate a typical outcome (e.g., in terms of number of modes) from a campaign of dedicated observations. The artificial data set is finalized by adding to the frequency of each selected mode a random perturbation that follows a normal (Gaussian) distribution. The mean value,  $\mu$ , of the normal deviates is set to zero in all our tests (implying that no bias is introduced in the perturbations), while the standard deviation,  $\sigma$ , is set to the desired value to mimic, e.g., random noise fluctuations in the frequency measurements. Three representative cases corresponding to different levels of precision are investigated. The first case is made comparable to the typical period fit precision achieved currently in the field, which is obtained by setting the standard deviation to  $\sigma = 10 \mu\text{Hz}$ . The second test case corresponds to a precision that would be limited by the accuracy of standard ground-based data, which is of the order of  $0.1 \mu\text{Hz}$  on the measured frequencies (hence,  $\sigma = 0.1 \mu\text{Hz}$ ). The third and last case represents the ultimate situation where the precision is only limited by the accuracy offered by *Kepler* data, which can reach down to  $\sim 1 \text{ nHz}$  on the measured frequencies for the longest runs and most stable pulsators (therefore,  $\sigma = 0.001 \mu\text{Hz}$ ).

From these modified subsets of periods, the objective is then to retrieve the global and shape parameters of the artificial reference star with our optimization tools. The latter have been described in some detail, in a white dwarf context, by Giammichele et al. (2016) who used them extensively for the analysis of the two ZZ Ceti stars R548 et GD 165. In a nutshell, our approach is a double optimization procedure that both matches the observed periods to computed periods assuming no a priori knowledge of the mode identification and conducts a multimodal global search of the best fit solution(s) in the vast model parameter space. The global optimization is carried out by the code LUCY, a robust hybrid genetic

algorithm capable of identifying and exploring simultaneously, if needed, several minima of the merit function in case the problem turns out to be ill-posed with no uniquely defined solution. Among other benefits, these tools ensure that the search is *objective* in the sense that the whole parameter space is thoroughly searched, the global minimum of the merit function is robustly found, and the uniqueness (or not) of the solution is assessed.

Along with these precision tests, three parametrizations are also experimented. The first set of tests is performed with a simple variable homogeneous core, while the second set uses the new one-transition parametrization, and the third set the two-transition parametrization.

A last test is performed highlighting the flexibility of the two-transition parametrization, by reproducing a reference star with a triple transition of He/C/O in its core with a rather thick helium layer this time, to emphasize that this parametrization is capable of mimicking models from evolutionary calculations.

### 3.1. Parametrization with a Varying Homogeneous Core

The different sets of “observed” periods are initially computed from a reference model with the parameters given in Table 1. This model represents a standard ZZ Ceti star, with a rather thick hydrogen envelope. As mentioned before, once the pulsation periods are calculated from the reference model, a subset of modes is selected, and their periods are perturbed with normally distributed (Gaussian) random fluctuations to the level of the chosen precision. This process is detailed in Table 2 which provides the values of the periods at all stages. The first column shows the periods of the reference star, while the following columns list the modified periods for each degree of precision, now and hereafter dubbed “current fit” ( $\sigma = 10 \mu\text{Hz}$ ), “ground-based data” ( $\sigma = 0.1 \mu\text{Hz}$ ), and “*Kepler* data” ( $\sigma = 0.001 \mu\text{Hz}$ ) precision. We acknowledge that these sets of modified periods represent only one realization over a somewhat small number of modes of the random perturbations applied to the original model periods. Ideally, each experiment would have to be repeated multiple times with different realizations for a better statistical assessment of error propagations, but this is not feasible practically speaking due to the large computational resources needed by the optimization process for each asteroseismic analysis. For our purpose, however, which is to obtain an order-of-magnitude estimate of the uncertainties on the derived model parameters, our approach is sufficient. The global search range where the optimization is done is also indicated in Table 1 for each parameter. The explored domain is vast and virtually allows for any model configurations potentially encountered for ZZ Ceti stars.

Table 3 presents the stellar parameters derived from the three optimizations based on

the modified subsets of periods with various degrees of precision. Each entry has errors statistically calculated from the likelihood function (linked to the  $\chi^2$ -type merit function  $S^2$ ) that was sampled by the optimization code during the search for the best-fit models (see Giammichele et al. 2016 for more details on this procedure; see also Fig. 3). In test case 1 (current fit precision), all parameters are well retrieved with a precision that is generally between 0.1% and 2%, for an unweighted  $S^2$ -value of 9.1. The optimization is less sensitive to chemical profiles deeper than the envelope, in particular the central homogeneous oxygen value is only determined with a precision of 6%. The achieved level of precision for the derived stellar parameters is found comparable, as one could have anticipated, to the precision claimed by former analyses of white dwarf stars. This shows a quantitative consistency between the level of precision that is achieved on the stellar parameters and the overall quality of the period fit. This connection is further illustrated with the other tests. With ground-based data precision, the  $S^2$ -value of the best-fit solution reaches four orders of magnitude less, for a general improvement of a factor  $\sim 100$  in precision for most of the global stellar parameters. Another four orders of magnitude are gained on  $S^2$  by switching to *Kepler* data precision. The parameters of the reference model are retrieved to an impressive precision of  $\sim 0.0002\%$  in that case. The homogeneous core composition is still less precisely determined by one order of magnitude compared to the other stellar parameters.

As a complementary view, Figures 4, 5 and 6 depict the maps of the projected merit function  $S^2$  (on a logarithmic scale) onto the  $T_{\text{eff}}\text{-log } g$  and  $D(\text{He})\text{-}D(\text{H})$  planes, as well as the derived probability density function of all the retrieved stellar parameters when considering the current fit precision ( $\sim 10\ \mu\text{Hz}$ ), the typical ground-based data ( $\sim 0.1\ \mu\text{Hz}$ ), and the *Kepler* precision ( $\sim 0.001\ \mu\text{Hz}$ ), respectively. White contours show regions where the period fits have  $S^2$ -values within the 1- $\sigma$ , 2- $\sigma$ , and 3- $\sigma$  confidence levels relative to the best-fit solution. The gain in precision for the derived stellar parameters, from current fit to *Kepler* data precision, is clearly illustrated from the inspection of the 2-D maps. With current fit precision (Fig. 4), the best-fit solution within 1- $\sigma$  is partly diluted in the background noise. With increasing observational precision, we get much narrower confidence level regions in the 2-D maps from Figures 5 and 6, as well as much narrower probability distributions for all stellar parameters, in line with the values given in Table 3 derived from these distributions.

### 3.2. Core Parametrization with One Transition Zone

The same exercise is conducted bearing in mind the use of the new parametrization. The reference star is this time computed with the adjustable core composition using a single transition. The global and shape parameters for that model are given in Table 4. The

pulsation periods for  $\ell = 1$  and 2  $g$ -modes for this reference star are then computed and perturbed using the same technique as described in the prior section. The modified subsets of periods corresponding to the three test cases, which allow investigating different levels of precision on the “measured” periods, are provided in Table 5.

In test case 1, where we lean toward the precision of current fits, we obtain after the optimization procedure a best fit solution with a  $S^2$ -value of 3.1, i.e., the same order of magnitude as previously found from our test with the homogeneous core. The estimated errors on the retrieved global and shape parameters given in Table 6 (second column, for test case 1) are slightly larger than the previous parametrization with the homogeneous core, but remain of the same order of magnitude. The optimization appears less sensitive to the shape parameter  $\Delta t_1$ , as the error on the value of this specific parameter reaches 20 %. We note from the tabulated values compared to the original model parameters given in Table 4 that the optimal solution uncovered in this case is slightly offsetted (by up to  $\sim 2\sigma$ ) relative to the true solution. We briefly discuss this feature below. As we move to a higher achievable period fit precision with test case 2, corresponding to a standard deviation from the original periods set of  $\sigma = 0.1 \mu\text{Hz}$ , the increase in precision for the derived model parameters is remarkable. The best-fit solution now matches the periods with an unweighted  $S^2$ -value of  $3.0 \times 10^{-4}$  and gives error on the stellar parameters of the order of  $\sim 0.01\%$ . If seismic analyses were only limited by the precision of the frequencies measured from typical ground-based observations, we would reach an impressive internal precision of 0.05 % for the determination of the mass, for example. Shape parameters are found to be less precisely determined, with errors of the order of 0.1-1%. Quite interestingly, the offset pointed out in the previous experiment has now disappeared, all seismically derived values matching the true values within  $1\sigma$ . With the typical *Kepler* precision, we gain a factor of a hundred relative to the achieved precision with ground-based data. The best  $S^2$ -value obtained in that particular test case 3 is  $6.1 \times 10^{-7}$  and the errors on the global parameters reduce further to  $\sim 0.0002\%$ , as for the seismic mass measurement. As before, the shape parameters, the core oxygen central value and  $\Delta t_1$ , are less precisely measured than the global parameters, while the transition  $t_1$  is well retrieved. This most certainly reflects the fact that the probing modes bear a lower sensitivity to this particular region of the star.

Figures 7, 8 and 9 show as before the maps of the projected merit function  $S^2$  (in logarithmic scale) onto the  $T_{\text{eff}}\text{-log } g$  and  $D(\text{He})\text{-}D(\text{H})$  plane as well as the probability density functions of all the retrieved stellar parameters for the current fit ( $\sim 10 \mu\text{Hz}$ ), typical ground-based data ( $\sim 0.1 \mu\text{Hz}$ ), and *Kepler* data ( $\sim 0.001 \mu\text{Hz}$ ) precisions, respectively. The 2-D maps of Figure 7 show a slightly shifted solution, if we only consider the  $1\text{-}\sigma$  region, but fall well within the  $2\text{-}\sigma$  region. This is related to the small shift already pointed out from the values given in Table 6. The probability distributions for each measured parameters also

illustrate this shift, providing additional insight on its origin. Indeed, for several parameters, the distribution appears bi-modal, with a main peak corresponding to the optimal (but slightly offsetted relative to the true model) solution, and smaller secondary peaks (a local minimum) that fall almost exactly on the true values. We have here an example of two close minima of the merit function, where the dominating solution (global minimum) is not necessarily the true solution (although not very different in the present case). Interestingly, this test case offers an illustration of the ambiguity and biases that can potentially arise in the seismic solution when the reached precision on the period fit is not sufficient. We also point out that a slight bias in the solution may also be generated by the fluctuations in the random numbers applied to the relatively few selected periods (small number statistics), which can tip the balance towards a specific region. This effect could eventually be compensated by repeating many times the same experiment (for better statistics), a refinement that we do not however implement in our present tests because of the very high computational burden it would imply. Hence, if we consider only the precision of the current fits, we can see that the determination of the solution may be affected by the background noise and potential secondary optima. We note also, based on the histograms, that the seismic optimization is clearly not sensitive enough to the parameter  $\Delta t_1$  at this level of precision. When increasing the precision on the measured frequencies, from typical ground-based data to *Kepler* data precision, we obtain much narrower confidence level regions in the 2-D maps as shown in Figures 8 and 9, as well as much narrower probability distributions for all stellar parameters, including the shape parameters of the core. This is in line with the values provided in Table 6 that derive from these distributions. We point out again that the small offsets relative to the true values have disappeared with the increased precision in the period fit, and secondary structures are no longer visible in the histograms. The latter shows that the best cure against potential ambiguities in the solution is an overall increase in the quality of the period fit.

Overall, we conclude this section by emphasizing that the new adjustable core parametrization used in the single-transition setup behaves well under the seismic analysis and allow to retrieve with a remarkable precision both the stellar and shape parameters of the reference star.

### 3.3. Core Parametrization with Two Transition Zones

For the last test of this series, we use the full potential and flexibility of the new core parametrization with the two-transition setup, both for the reference star and the global search. The parameters defining the standard reference star are provided in Table 7, along with the search range considered for the optimizations. The pulsation periods for dipole and



quadrupole  $g$ -modes are again computed from this reference model, and then modified using the same technique described earlier. The perturbed subsets of periods used for the three test cases corresponding to the different levels of precision are given in Table 8.

We find, as summarized in Table 9, that the seismic measurements of the global and shape parameters follow the same pattern as in the two previous experiments involving a homogeneous core of variable composition and a stratified core with the one-transition parametrization. The internal precision on the seismically derived model parameters improves by an important factor of  $\sim 100$  at each step from the current fit precision to typical ground based data and *Kepler* data precisions. If we examine more closely Table 9, we notice that shape parameters are less precisely determined, especially  $\Delta t_1$  and  $\Delta t_2$  for which the error on the obtained value reaches up to  $\sim 30\%$ , in the least favorable test case based on current fit precision. This situation improves as we achieve higher precision for the period fits. In particular, we find that to accurately constrain the shape parameters defining the core structure, the overall precision of the seismic fit must be able to reproduce the observed periods at least to the precision of  $\sim 0.1 \mu\text{Hz}$  (test case 2). In retrospect, this should not be very surprising considering that the modes are usually less sensitive to structures in the core, meaning that precise fits are needed to capture correctly their signature in the period spectrum of the star. Otherwise, these signatures are simply blurred or hidden by the noise.

Figures 10, 11, and 12 again illustrate the solutions with maps of the projected merit function  $S^2$  onto the  $T_{\text{eff}}\text{-log } g$  and  $D(\text{He})\text{-}D(\text{H})$  plane, as well as probability density functions derived for all the retrieved stellar parameters for the current fit ( $\sim 10 \mu\text{Hz}$ ), typical ground-based data ( $\sim 0.1 \mu\text{Hz}$ ) and *Kepler* ( $\sim 0.001 \mu\text{Hz}$ ) precision levels, respectively. The 2-D maps in Figure 10 (current fit precision test case) present again a slightly shifted minimum compared to the true values, if we stay strictly within the  $1\text{-}\sigma$  region, but consistency with the true model is achieved well within the  $2\text{-}\sigma$  region. The probability distribution functions (histograms) show that the seismic optimization is clearly not sensitive enough to the parameter  $\Delta t_1$  and  $\Delta t_2$  at this level of precision. Increasing the fit precision to the level of typical ground-based data and *Kepler* data leads to much narrower confidence level regions in the 2-D maps, as illustrated in Figures 11 and 12, as well as much narrower probability distributions for all stellar parameters. We also observe, in Figure 11 (typical ground-based data precision), the presence of a weak secondary solution (visible on some histograms, but not at the scale of the 2-D maps) slightly offsetted from the main peaks and the true values. It disappears when considering fits that can reproduce the observed periods with a greater accuracy (see Figure 12). If all the parameters are now found to be well constrained, we nevertheless note that the values of the majority of the shape parameters from the reference star do not fall within the  $1\text{-}\sigma$  limits of the probability distribution of the recovered parameters. This bias is most notably visible in Figure 12 (typical *Kepler* data precision). We

trace down this problem to an under-sampling of the merit function in the vicinity of the solution by the optimization code. The parameter space volume to explore indeed increases considerably with the addition of more parameters to define a 2-transition core. This can be balanced by scaling the optimizer resources to the size of the problem considered (at the cost of an increase of the needed computational resources) but, for simplicity and to save on our limited (in terms of available CPU time) computer resources, the genetic algorithm was used with the same initial population of 1,000 evolved solutions for all the tests with different parametrizations. Therefore, the error estimates in the most demanding cases (and the most demanding experiment is the one shown in Figure 12) may be underestimated for some parameters. This being said, a quick look at the scales involved in each histogram shows that the bias is extremely small and the issue is minor.

### 3.4. The Special Case When a Triple He/C/O Transition Exists

The choice of a relatively thin layer of helium to compute the reference models for our testing purposes is one of the many possible configurations allowed by the new parametrization. However, it does not allow to see the triple transition of He/C/O noticed in models computed from evolutionary means that have rather thick helium mantles. To show that the parametrization is nonetheless capable of mimicking this feature and to assess that the precision obtained is comparable to the case previously presented with a thinner layer of helium with the two-transition parametrization, we deal with a last test case. We use again the new core parametrization with the two-transition zones, but this time having the precise setup of a triple transition of He/C/O at the edge of the core for the reference star. The parameters defining the standard reference star are provided in Table 10. No restrictions whatsoever are applied to the search parameters, e.g. the search range is wide enough to accommodate thin or thick helium layers with or without a triple transition of He/C/O, as can be seen from the search range exposed in Table 10. For this last test, we only look at the most stringent case, by using the level of precision given by the *Kepler* data. Pulsations periods for dipole and quadrupole  $g$ -modes are again computed from the reference model, and then modified using the same technique as described earlier. The perturbed subset of periods used for this last test case corresponding to the *Kepler* level of precision is given in Table 11.

The seismic measurements of the global and shape parameters follow exactly the same pattern as previously presented in the experiment involving a stratified core with the two-transition parametrization and a thin helium layer, as summarized in Table 12. If we look more into details, the internal precision reached for the seismically derived parameters is

similar in all points to what was previously found for the stratified core with the two-transition parametrization and the thin helium layer, if we compare to the test case 3 in Table 9. Periods, global and shape parameters are reproduced to the same precision. We still observe that shape parameters are less accurately determined than global parameters, an effect of the lesser sensitivity of the probing modes onto the structures in the core.

Figure 13 illustrates the internal chemical profiles (top panel) of the reference star (red curves) with a thick helium layer and a triple transition of He/C/O, superimposed with the chemical profiles retrieved from the optimization (black curves). The bottom panel presents the run of the Brunt-Väisälä frequency as well as the Lamb frequencies for both the reference and the retrieved model. We can only notice the perfect superposition of the two models on both panels, demonstrating that the parametrization and our optimization tools are equally capable of retrieving models with thick helium layer that involves a triple transition of He/C/O at the core boundary.

In summary, we have demonstrated that our optimization procedure is perfectly capable of retrieving the stellar and shape parameters from a reference star for different configurations and for different levels of precision in fitting the periods measured from seismic observations. If the limiting factor was purely observational, that is governed only by the actual precision on the measured frequencies (or periods), we find that stellar and shape parameters could be recovered to an outstanding internal precision, much higher than currently obtained. This result illustrates the very strong potential offered by asteroseismology which still has to be fully exploited. Although our asteroseismic method gives robust, precise, and accurate constraints on either stellar or shape parameters, the current limiting factor is usually not the precision of the observations but the uncertainties associated with the constitutive physics included in the models. The latter need to be addressed in order to go beyond current achievements in white dwarf asteroseismology, especially if we aim at setting better constraints on the core chemical profiles which is only possible if we significantly improve the overall quality of the obtained seismic fits compared to current standards.

#### 4. TESTS WITH RANDOM PERIOD SEQUENCES

In this section, we present additional tests using randomly generated period sets. When we perform a seismic analysis, the optimization process is governed by the minimization of a merit function. During the optimization, the merit function will take on different values as we search in parameter space. The point here is that there will always be a minimum value found at the end of the process, but this minimum value is not necessarily statistically significant. The proposed tests allow us to roughly estimate a threshold on the best-fit value

of the merit function over which a random set of periods could likely be fitted equally well. Hence, this threshold indicates when a seismic analysis is credible or not, based on the overall quality of the obtained period fit. Obviously, such tests should be performed a large number of times and for different observed mode configurations in order to get significant statistics and a truly global overview of the problem. However, because we are mostly interested here in getting a rough idea of this threshold in the context of the experiments conducted in this paper and because calculating power and time was limited for this project, we only perform this test five times for each core parametrization presented earlier. We point out that, ideally, this kind of experiment should be done (and tuned) for each specific seismic analysis of a pulsating white dwarf star in order to assess the reliability of the results.

In the following experiments, ten periods are randomly computed with the only restriction that they fall between 100 and 500 seconds in order to remain in the same range as the previous tests and calculations. Five random tests are performed, and the pulsation spectra used in each case are given in Table 13.

The results of the five test cases conducted for each core parametrization are presented in Table 14. The merit function  $S^2$ , an unweighted  $\chi^2$ , as well as  $\langle \Delta\nu \rangle$ , the average frequency dispersion, and  $\langle \Delta P \rangle$ , the average period dispersion of the best-fit solution are disclosed. The first observation that can be made out of this test, when we go through the columns, is that the values of either  $S^2$ ,  $\langle \Delta\nu \rangle$  and  $\langle \Delta P \rangle$  are greatly varying. But, again, since we are just interested in an estimation of the threshold for a credible seismic analysis, these five test cases are sufficient for having a rough idea of the value of  $S^2$  above which the fit must be considered as not statistically significant. The second observation is that the increase in flexibility of the core definition from the varying homogeneous core to the one- and two-transition parametrization leads to an overall decrease of the values obtained from these random tests. Therefore, not surprisingly, the threshold is not the same if we use an homogeneous core or a more complex core chemical profile parametrization, being more stringent in the latter case.

With the varying homogeneous core, the best-fit merit value went down to as low as  $\sim 15$  (Case 5; see Table 14), even though the average value of the 5 tests is quite higher. The corresponding average period dispersion is around  $\langle \Delta P \rangle \sim 2$  s. With the one- and two-transition parametrizations, the dispersion between the values obtained for each random test is less important. The average value for  $S^2$  is of the order of ten. In these cases, the average period difference of the best-fit solution becomes less than 1 s. Hence, depending on the parametrization used, we can define a conservative limit of about 1 s on the average period dispersion between the optimal model and the observations above which a seismic solution becomes essentially meaningless, considering that it could have reproduced a random period

spectrum equally well. This finding, although needing to be tuned to each specific analysis for a more precise quantitative statement, is of importance to judge the reliability of past and future asteroseismic inferences of white dwarf stellar properties.

## 5. TESTING THE CORE PARAMETRIZATION WITH A STRATIFICATION FROM EVOLUTIONARY MODELS

In this section, we investigate the flexibility of the new parametrization and its capability to reproduce the chemical stratification derived from standard evolutionary models. For this test, we start with a static model using the chemical profiles in the core derived from Maurizio Salaris’ evolutionary models. The core profile is obtained by interpolating between the available profiles derived for different masses by Salaris et al. (2008). The resulting core profile is then smoothed out to remove as much as possible the numerical noise still unfortunately present in the resulting curve. This reference model has the global parameters listed in Table 15.

The resulting chemical profiles as well as the Brunt-Väisälä and Lamb frequencies for  $\ell = 1$  and  $\ell = 2$  are illustrated in Figure 14. We can still observe some noisy features in the Brunt-Väisälä frequency which are most probably residuals from the numerical noise that was propagated during the evolution in the pre-white dwarf phases.

Table 16 (first column) presents the “observed” periods and mode identification chosen from the reference model. A set of ten periods were selected: five dipole modes with consecutive values of the radial order  $k$  from 2 to 6, and a similar group of five quadrupole modes with  $k$  ranging from 3 to 7. These modes were chosen in order to best represent ZZ Ceti stars close to the blue edge of the instability strip. Also, we made sure that our choice would include modes that probe the deep interior, a property that is confirmed in Figure 15 showing the weight functions of the selected modes. These modes are the equivalent of the deeply confined modes discovered in Ross 548 (Giammichele et al. 2016), and their presence in the “observational” data considered here is of course necessary for testing our different core parametrizations. The ultimate test is then to try to recover the global parameters and structure of the reference model (the white dwarf defined with a core composition derived from evolution calculations) from the pulsations periods, with chemical profiles in the core defined by the different levels of sophistication of our parametrization. It is important to realize that this experiment differs from the tests presented in prior sections in that the structure to recover cannot be exactly reproduced even by our most flexible 2-transition parametrization of the core. Only the main features of the chemical profiles can be approximated. This test is therefore more stringent for evaluating the overall robustness of the

method.

The first experiment consists of using the simplest parametrized static model we have, the varying homogeneous core, to search for a best-fit solution matching the “observed” periods. The search range used in the optimization process for every parameter of interest is indicated in Table 15. The resulting global parameters for this first test are given in Table 17, and the associated chemical profiles are illustrated in Figure 16 (black curves) relative to the reference model (red curves). The  $S^2$ -value of 17.5 obtained for the best solution is somewhat high and has to be considered carefully as it reaches some of the values obtained in the random tests described in the previous section. A close examination of Table 16 reveals, however, that a substantial part of this large value of  $S^2$  is due to the particularly poor mismatch between the theoretical and “observed” period for the mode with  $\ell = 1$  and  $k = 6$ . Otherwise, the period fits for the nine other modes are quite acceptable. We point out that four out of the ten modes of interest have not been identified correctly in terms of their defining indices  $\ell$  and  $k$ . And, of course, the detailed composition profile of our reference model cannot be reproduced in the context of this first test with homogeneous cores. This is well illustrated in Figure 16. Despite these shortcomings, and perhaps somewhat surprisingly, the hypothesis of an homogeneous core still leads to quite reasonable estimates of the global structural parameters of the reference model as can be observed in Table 17. We recall in this context that the hypothesis of homogeneous cores has proven itself a good approximation in the cases of GD 165 – in particular – and Ross 548 for which the six observed periods were well fitted for each star (Giammichele et al. 2016). We also remind the reader here that the current set of ten periods was specifically chosen to probe deep into the reference star, since we were mainly concerned in showing the improvement brought up by the new parametrization.

A substantial gain on all fronts is obtained by using parametrized cores defined by three parameters and corresponding to a chemical profile with a single transition zone. This parametrization, a particular case of the complete two-transition model, is obtained by setting  $t1_o$  and  $t2_o$  to zero,  $\Delta t2$  to a non-zero value and  $t2$  fixed at  $-2.0$ , far enough that it does not interfere within the range of  $t1$ . Table 17 reveals a clear improvement of the merit function, from  $S^2 = 17.5$  to  $10.4$ , and the average dispersion in period,  $< \Delta P >$ , has dropped below 1 s. In both cases, much of the deviation is dominated by a particularly poor mismatch, this time associated with the  $\ell = 2$  and  $k = 7$  mode (see Table 16). The period fits are quite acceptable for the nine other modes. In addition, the mode identification is this time perfectly recovered and the global parameters of the solution are noticeably closer to the ones from the reference model. A look at Figure 17 also reveals a clear improvement in the resemblance of the Brunt-Väisälä frequency with the one of the reference model. The first core feature is almost perfectly positioned at the first transition, along with the two chemical



transitions between the core and the helium-rich mantle, and between the helium layers and the hydrogen envelope. The central values of carbon and oxygen are somehow inverted, a rather striking result, but since this inversion does not reflect strongly on the Brunt-Väisälä frequency (inverting the values of  $X(C)$  and  $X(O)$  leads to a very similar profile), the sensitivity of the period-fitting optimization process to this parameter is certainly weak. Therefore it most probably cannot be well constrained in view of the still relatively high  $S^2$ -value of the best-fit solution. The latter is almost entirely due to the absence of the second feature in the core corresponding to the second drop in the oxygen profile, but the chemical stratification is overall quite well reproduced with the one-transition parametrization.

At this stage, the need for a two-transition parametrization should be clear. The Salaris profile presents two major drops in the oxygen stratification, so it is most natural to try to recover the reference model with a two-transition core parametrization. The advantage of a more flexible parametrization at this level is expected to be visible through an improved value of  $S^2$  and, therefore, a better match between the “observed” periods of the reference model and the computed theoretical periods. The question remaining is how accurately the periods and the chemical profiles in the core can be reproduced.

As above, the results of this third test are presented in Table 17. The  $S^2$ -value of 0.1 and the average  $\langle \Delta P \rangle$  of 0.09 s obtained for the best-fit model are, respectively, two and one orders of magnitude smaller than previously achieved with the variable homogeneous core and the one-transition parametrization. This corresponds to an impressive improvement, which demonstrates that our prescription can indeed mimic quite well, although not perfectly, the complex chemical stratification expected in the cores of white dwarf stars. By inspecting the theoretical periods matched to the periods of the reference model in Table 16, we note that the period 376.01 s is wrongly identified. However, a closer inspection of the model shows that the correct identification would have only very slightly increased the merit function  $S^2$ , because the value of the  $\ell = 1, k = 6$  mode period is almost identical to the  $\ell = 2, k = 12$  mode period. Beside this very minor problem, the global atmospheric parameters of the reference star are significantly better constrained than before, save for the helium layer mass.

Finally, inspecting Fig. 18 shows that the two-transition prescription for the oxygen profile matches rather well the original oxygen profile taken from Salaris et al. (2008). The central homogeneous values of the oxygen and carbon mass fractions are correctly recovered, and the two transitions are perfectly placed. The layering of the helium and the hydrogen envelope is well superimposed on the chemical profiles of the reference model. The exact shapes of the first and, mostly, the second feature of the Brunt-Väisälä frequency corresponding to the reference model are not so well matched, but this does not seem a major

problem as the periods and the overall model are finely reproduced. The shape of these inner transitions most likely have a smaller impact than other structures on the period spectrum and would require higher precision period fits to be more accurately reproduced.

In summary, with this test, the flexibility of the new two-transition core parametrization was explored and proven to be sufficient, as well as necessary, to recover sufficiently accurately the details of the complex chemical stratification expected from evolutionary calculations. Global parameters can be estimated fairly reliably from the approximation of homogeneous cores, but this has to be handled with care, especially when the modes probe deeper than the envelope of the star. To best reproduce the core chemical profile, the two-transition parametrization is necessary and cannot be replaced by the simpler one-transition setup.

## 6. CONCLUSION

In this paper, we introduced and tested a new parametrization that can replicate smoothly one or two steep "drops" in the chemical profile of oxygen in the core of a white dwarf model in order to better reproduce the shape of the stratification usually predicted from evolutionary models. The flexibility of the new two-transition core parametrization was explored and proven to be both necessary and sufficient for recovering the structure expected from evolutionary calculations. To be clear, the evolutionary structures are not reproduced to perfection, but we showed that the method is amply sufficient for testing the most important features of the chemical profile of a white dwarf through asteroseismology. And if need be, in special cases, the flexibility of our approach could also be improved. This new parametrization will be of high interest in upcoming seismic studies of pulsating white dwarfs, particularly those with available *Kepler* and *K2* data, which we plan to analyze thoroughly with our optimization tools developed for asteroseismology.

For the future, we retain the following lessons from the current work. Based on tests generated with random sequences of periods, we can roughly define a conservative threshold of  $\sim 1$  s for the average period dispersion of the best-fit solution above which results from seismic analyses should not be considered as very robust (i.e., statistically significant). We showed that our seismic method, based on parametrized models in hydrostatic equilibrium, is perfectly capable of retrieving stellar and shape parameters from a reference star with different levels of precision in the "observational" data. If the limiting factor was purely observational, i.e., only governed by the errors in measuring the pulsation frequencies (periods), stellar and shape parameters could be recovered to a remarkable precision. However, although our asteroseismic method gives robust, precise, and accurate constraints on both stellar or shape parameters, the limiting factor is usually not the precision of the observa-

tions themselves, but the uncertainties associated with the constitutive physics involved in current stellar models which still dominate the error budget. The latter need to be addressed in order to go beyond current achievements and improve overall the quality of the seismic fits toward solutions that approach the very stringent limit of observational measurement errors.

This work was supported in part by the NSERC Canada through a doctoral fellowship awarded to Noemi Giammichele, and through a research grant awarded to Gilles Fontaine. The latter also acknowledges the contribution of the Canada Research Chair Program. Stéphane Charpinet acknowledges financial support from “Programme National de Physique Stellaire” (PNPS) of CNRS/INSU, France, and from the Centre National d’Études Spatiales (CNES, France). This work was granted access to the HPC resources of CALMIP under allocation number 2015-p0205.

## REFERENCES

- Akima, H. 1970, JACM, Vol. 17, No. 4, 589
- Althaus, L. G., Serenelli, A. M., Córscico, A. H., & Benvenuto, O. G. 2002, MNRAS, 330, 685
- Althaus, L. G., Córscico, A. H., Bischoff-Kim, A., et al. 2010, ApJ, 717, 897
- Baglin, A., Auvergne, M., Barge, P., et al. 2009, IAU Symposium, 253, 71
- Bell, K.J., Hermes, J.J., Bischoff-Kim, A., et al. 2015, ApJ, 809, 14
- Bischoff-Kim, A., Østensen, R., Hermes, J.J., & Provencal, J.L. 2014, ApJ, 794, 39
- Bradley, P. A. 1996, ApJ, 468, 350
- Bradley, P. A. 1998, ApJS, 116, 307
- Bradley, P. A. 2001, ApJ, 552, 326
- Brassard, P., Fontaine, G., Wesemael, F., & Hansen, C. J. 1992, ApJS, 80, 369
- Castanheira, B. G., & Kepler, S. O. 2008, MNRAS, 385, 430
- Castanheira, B. G., & Kepler, S. O. 2009, MNRAS, 396, 1709
- Chen, Y. H. 2016, MNRAS, 458, 1190

- Córsico, A. H., Althaus, L. G., Miller Bertolami, M. M., & Bischoff-Kim, A. 2012, *A&A*, 541, A42
- Fontaine, G., & Brassard, P. 2002, *ApJ*, 581, 33
- Gallart, M.S. 2002, M.Sc. thesis, Development of a Design Tool for Aerodynamic Shape Optimisation of Aerofoils, Department of Mechanical Engineering, University of Victoria
- Charpinet, S., Van Grootel, V., Brassard, P. et al. 2013, in *EPJ Web of Conf.*, Aging Low Mass Stars: From Red Giants to White Dwarfs, ed., A. Noels & V. Van Grootel, 43, 04005
- Giammichele, N., Fontaine, G., Brassard, P., & Charpinet, S. 2015, *ApJ*, 815, 56
- Giammichele, N., Fontaine, G., Brassard, P., & Charpinet, S. 2016, *ApJS*, 223, 10
- Gilliland, R.L., Brown, T.M., Christensen-Dalsgaard, J., et al. 2010, *PASP*, 122, 131
- Greiss, S., Gänsicke, B.T., Hermes, J.J., et al. 2014, *MNRAS*, 438, 3086
- Greiss, S., Gänsicke, B.T., Hermes, J.J., et al. 2015, 19th European Workshop on White Dwarfs, 493, 169
- Hermes, J.J., Mullally, F., Østensen, R.H., et al. 2011, *ApJ*, 741, L16
- Hermes, J.J., Charpinet, S., Barclay, T., et al. 2014, *ApJ*, 789, 85
- Landolt, A.U. 1968, *ApJ*, 153, 151
- Matthews, J.M. 2007, *Communications in Asteroseismology*, 150, 333
- Mazzitelli, I., & D’Antona, F. 1986, *ApJ*, 308, 706
- Mazzitelli, I., & D’Antona, F. 1986, *ApJ*, 311, 762
- Metcalf, T. S. 2005, *MNRAS*, 363, L86
- Michel, E., Baglin, A., Auvergne, M., et al. 2008, *Science*, 322, 558
- Østensen, R.H., Silvotti, R., Charpinet, S., et al. 2011, *MNRAS*, 414, 2860
- Østensen, R.H., Bloemen, S., Vučković, M., et al. 2011, *ApJ*, 736, L39
- Romero, A.D., Córsico, A.H., Althaus, L., et al. 2012, *MNRAS*, 420, 1462

- Salaris, M., Domínguez, I., García-Berro, E., et al. 1997, ApJ, 486, 413
- Salaris, M., Cassisi, S., Pietrinferni, A. et al. 2010, ApJ, 716, 1241
- Straniero, O., Domínguez, I., Imbriani, G., & Piersanti, L. 2003, ApJ, 583, 878
- Tassoul, M., Fontaine, G., & Winget, D.E. 1990, ApJS, 72, 335
- Van Grootel, V., Charpinet, S., Brassard, P., Fontaine, G., & Green, E.M. 2013, A&A, 553, A97
- Wood, M. A. 1992, ApJ, 386, 539

Table 1: Parameters of the reference star as well as the search range for the optimization with a variable homogeneous core.

Parameter	Value	Search range
$T_{\text{eff}}$ (K)	12,000	11,000 - 13,000
$\text{Log } g$	8.00	7.80 - 8.20
$D(\text{H})$	−5.0	−9.0 - −4.0
$D(\text{He})$	−3.0	−4.0 - −1.5
Total mass ( $M_{\odot}$ )	$5.9479 \times 10^{-1}$	...
Radius ( $R_{\odot}$ )	$1.2765 \times 10^{-2}$	...
Core oxygen fraction (%)	50	0 - 100



Table 2: Selected and modified periods for the reference star with a variable homogeneous core.

$\ell$	$k$	Period (s)	$\sigma = 10 \mu\text{Hz}$	$\sigma = 0.1 \mu\text{Hz}$	$\sigma = 0.001 \mu\text{Hz}$
1	1	151.53791917	...	...	...
1	2	<b>227.016706244</b>	<b>226.98946604</b>	<b>227.01643381</b>	<b>227.01670352</b>
1	3	<b>313.807911837</b>	<b>313.66203636</b>	<b>313.80645241</b>	<b>313.80789724</b>
1	4	<b>325.278884448</b>	<b>325.58422098</b>	<b>325.28193498</b>	<b>325.27891495</b>
1	5	<b>379.026095735</b>	<b>380.55088833</b>	<b>379.04128317</b>	<b>379.02624760</b>
1	6	<b>436.100785261</b>	<b>433.16916032</b>	<b>436.07127260</b>	<b>436.10049011</b>
1	7	459.45372755	...	...	...
2	2	131.65045899	...	...	...
2	3	<b>181.920837778</b>	<b>181.85326019</b>	<b>181.92016175</b>	<b>181.92083102</b>
2	4	<b>212.206268924</b>	<b>212.35274848</b>	<b>212.20773272</b>	<b>212.20628356</b>
2	5	<b>224.636765373</b>	<b>224.25083274</b>	<b>224.63289947</b>	<b>224.63672671</b>
2	6	<b>260.460240785</b>	<b>259.40908188</b>	<b>260.44968703</b>	<b>260.46013524</b>
2	7	<b>282.114308484</b>	<b>283.05460137</b>	<b>282.12368049</b>	<b>282.11440220</b>
2	8	306.14572754	...	...	...
2	9	336.77469004	...	...	...
2	10	357.86963676	...	...	...
2	11	387.57588290	...	...	...
2	12	414.11284901	...	...	...
2	13	437.72710109	...	...	...
2	14	467.36842954	...	...	...
2	15	491.40529857	...	...	...

Table 3: Results from the three optimizations searching for the reference star with a variable homogeneous core and with different levels of precision: current fit precision, ground-based data and *Kepler* data precision.

	Test case 1	Test case 2	Test case 3
	$\mu = 0$ , $\sigma = 10 \mu\text{Hz}$	$\mu = 0$ , $\sigma = 0.1 \mu\text{Hz}$	$\mu = 0$ , $\sigma = 0.001 \mu\text{Hz}$
$S^2$	9.1	$9.1 \times 10^{-4}$	$9.2 \times 10^{-8}$
$< \Delta\nu > (\mu\text{Hz})$	8.29	0.083	0.0083
$< \Delta X/X > (\%)$	0.24	$2.35 \times 10^{-3}$	$2.37 \times 10^{-5}$
$T_{\text{eff}}$ (K)	$11,970 \pm 140$ (0.3 %)	$12,000.5 \pm 4.0$ (0.0042 %)	$11,999.99 \pm 0.06$ (0.0001 %)
Log g	$8.008 \pm 0.030$ (0.1 %)	$7.9999 \pm 0.0008$ (0.0012 %)	$8.00000 \pm 0.00001$ (0.0001 %)
$D(\text{H})$	$-5.03 \pm 0.15$ (0.6 %)	$-5.000 \pm 0.002$ (0.02 %)	$-5.00000 \pm 0.00004$ (0.0002 %)
$D(\text{He})$	$-3.07 \pm 0.10$ (2.3 %)	$-3.000 \pm 0.003$ (0.03 %)	$-3.00001 \pm 0.00004$ (0.0003 %)
Total mass ( $M_{\odot}$ )	$0.60 \pm 0.02$ (0.9 %)	$0.5948 \pm 0.0005$ (0.002 %)	$0.594791 \pm 0.000006$ (0.0002 %)
Radius ( $R_{\odot}$ )	$0.0127 \pm 0.0003$ (0.5 %)	$0.01277 \pm 0.00001$ (0.04 %)	$0.01276541 \pm 0.00000008$ (0.003 %)
Core oxygen fraction (%)	$53 \pm 8$ (6 %)	$50.0 \pm 0.3$ (0.2 %)	$50.001 \pm 0.003$ (0.002 %)

Table 4: Parameters of the reference star and search range for the optimization procedure using models with a one-transition core.

Parameter	Value	Search range
$T_{\text{eff}}$ (K)	12,000	11,000 - 13,000
$\text{Log } g$	8.00	7.80 - 8.20
$D(\text{H})$	−5.0	−9.0 - −4.0
$D(\text{He})$	−3.0	−4.0 - −1.5
Total mass ( $M_{\odot}$ )	$5.9593 \times 10^{-1}$	...
Radius ( $R_{\odot}$ )	$1.2778 \times 10^{-2}$	...
Core oxygen fraction (%)	70	0 - 100
$t_1$	−0.3	−0.50 - −0.15
$\Delta t_1$	0.06	0.010 - 0.10

Table 5: Selected and perturbed periods for the reference star with the one-transition core.

l	k	Period (s)	$\sigma = 10 \mu\text{Hz}$	$\sigma = 0.1 \mu\text{Hz}$	$\sigma = 0.001 \mu\text{Hz}$
1	1	151.75446102	...	...	...
1	2	<b>216.81536572</b>	<b>216.79051854</b>	<b>216.81511722</b>	<b>216.81536323</b>
1	3	<b>233.92848154</b>	<b>233.08021901</b>	<b>233.91996835</b>	<b>233.92839640</b>
1	4	<b>315.62545841</b>	<b>315.91293268</b>	<b>315.62833057</b>	<b>315.62548713</b>
1	5	<b>372.35739163</b>	<b>373.82889673</b>	<b>372.37204934</b>	<b>372.35753820</b>
1	6	<b>407.89150141</b>	<b>405.32576007</b>	<b>407.86568322</b>	<b>407.89124321</b>
1	7	456.09585372	...	...	...
2	2	133.59921893	...	...	...
2	3	<b>151.31237295</b>	<b>151.26561948</b>	<b>151.31190527</b>	<b>151.31236828</b>
2	4	<b>182.34310127</b>	<b>182.45124394</b>	<b>182.34418206</b>	<b>182.34311208</b>
2	5	<b>216.56591828</b>	<b>216.20719723</b>	<b>216.56232518</b>	<b>216.56588235</b>
2	6	<b>241.19856963</b>	<b>241.88556292</b>	<b>241.20542025</b>	<b>241.19863814</b>
2	7	<b>264.34846623</b>	<b>264.24494250</b>	<b>264.34743059</b>	<b>264.34845587</b>
2	8	299.27669790	...	...	...
2	9	328.49590688	...	...	...
2	10	350.35377602	...	...	...
2	11	385.35347602	...	...	...
2	12	407.54276181	...	...	...
2	13	422.40023701	...	...	...
2	14	447.50516837	...	...	...
2	15	475.14880300	...	...	...

Table 6: Results from the three optimizations from the reference star with a one-transition core and with different levels of precision: current fit precision, ground-based data and *Kepler* data precision.

	Test case 1	Test case 2	Test case 3
	$\mu = 0$ , $\sigma = 10 \mu\text{Hz}$	$\mu = 0$ , $\sigma = 0.1 \mu\text{Hz}$	$\mu = 0$ , $\sigma = 0.001 \mu\text{Hz}$
$S^2$	3.1	$3.0 \times 10^{-4}$	$6.1 \times 10^{-7}$
$\langle \Delta\nu \rangle (\mu\text{Hz})$	7.29	0.083	0.0043
$\langle \Delta X/X \rangle (\%)$	0.17	$1.90 \times 10^{-3}$	$9.52 \times 10^{-5}$
$T_{\text{eff}} (\text{K})$	$11,770 \pm 120$ ( 1.9 %)	$11,998.5 \pm 3.0$ ( 0.01%)	$11999.96 \pm 0.05$ ( 0.0003%)
$\text{Log } g$	$8.045 \pm 0.022$ ( 0.6 %)	$8.0006 \pm 0.0005$ ( 0.008%)	$8.000005 \pm 0.000008$ ( 0.0001%)
$D(\text{H})$	$-5.17 \pm 0.10$ ( 3.4 %)	$-5.002 \pm 0.02$ ( 0.04%)	$-5.00002 \pm 0.0000025$ ( 0.0004%)
$D(\text{He})$	$-3.15 \pm 0.06$ ( 5.0 %)	$-3.002 \pm 0.0012$ ( 0.07%)	$-3.00002 \pm 0.00002$ ( 0.0007%)
Total mass ( $M_{\odot}$ )	$0.62 \pm 0.01$ ( 4.0 %)	$0.5962 \pm 0.0003$ ( 0.05%)	$0.595930 \pm 0.000003$ ( 0.0002%)
Radius ( $R_{\odot}$ )	$0.0124 \pm 0.0002$ ( 3.0 %)	$0.012772 \pm 0.000004$ ( 0.05%)	$0.0127775 \pm 0.0000001$ ( 0.004%)
Core oxygen fraction (%)	$66 \pm 3$ ( 5.7 %)	$0.6998 \pm 0.0015$ ( 0.03%)	$0.70000 \pm 0.00002$ ( 0.001%)
$t_1$	$-0.300 \pm 0.018$ ( 0.3 %)	$-0.3003 \pm 0.0006$ ( 0.1 %)	$-3.00000 \pm 0.000008$ ( 0.0003%)
$\Delta t_1$	$0.072 \pm 0.015$ ( 20 %)	$0.0607 \pm 0.0015$ ( 1.2 %)	$0.060015 \pm 0.000013$ ( 0.03%)

Table 7: Parameters of the reference star and search range for the optimization using a two-transition core.

Parameter	Value	Search range
$T_{\text{eff}}$ (K)	12,000	11,000 - 13,000
$\text{Log } g$	8.00	7.80 - 8.20
$D(\text{H})$	−5.0	−9.0 - −4.0
$D(\text{He})$	−3.0	−4.0 - −1.5
Total mass ( $M_{\odot}$ )	$5.9521 \times 10^{-1}$	...
Radius ( $R_{\odot}$ )	$1.2770 \times 10^{-2}$	...
Core oxygen fraction (%)	70	0 - 100
$t_1$	−0.3	−0.50 - −0.15
$\Delta t_1$	0.06	0.010 - 0.10
$t_1$ oxygen (%)	40	0 - 100
$t_2$	−1.5	−2.00 - −0.60
$\Delta t_2$	0.08	0.010 - 0.10
$t_2$ oxygen (%)	20	0 - 100



Table 8: Selected and modified periods for the reference star with the two-transition core.

$\ell$	$k$	Period (s)	$\sigma = 10 \mu\text{Hz}$	$\sigma = 0.1 \mu\text{Hz}$	$\sigma = 0.001 \mu\text{Hz}$
1	1	151.653409370	...	...	...
1	2	<b>228.787742059</b>	<b>228.76007521</b>	<b>228.78746536</b>	<b>228.78773929</b>
1	3	<b>264.030696374</b>	<b>263.92742134</b>	<b>264.02966322</b>	<b>264.03068604</b>
1	4	<b>315.524781925</b>	<b>315.81207274</b>	<b>315.52765225</b>	<b>315.52481063</b>
1	5	<b>369.012046557</b>	<b>370.45717843</b>	<b>369.02644206</b>	<b>369.01219051</b>
1	6	<b>399.888135738</b>	<b>397.42178861</b>	<b>399.86332075</b>	<b>399.88788757</b>
1	7	455.034684809	...	...	...
2	2	133.361713913	...	...	...
2	3	<b>178.011613603</b>	<b>177.94690859</b>	<b>178.01096632</b>	<b>178.01160713</b>
2	4	<b>183.545746313</b>	<b>183.65532062</b>	<b>183.54684141</b>	<b>183.54575726</b>
2	5	<b>216.944553720</b>	<b>216.58457827</b>	<b>216.94094804</b>	<b>216.94451766</b>
2	6	<b>238.597497023</b>	<b>237.71509923</b>	<b>238.58864062</b>	<b>238.59740846</b>
2	7	<b>263.710718836</b>	<b>264.53215547</b>	<b>263.71890795</b>	<b>263.71080072</b>
2	8	298.974939191	...	...	...
2	9	327.792644523	...	...	...
2	10	348.111904002	...	...	...
2	11	380.831879546	...	...	...
2	12	405.577093095	...	...	...
2	13	427.351916311	...	...	...
2	14	445.672564712	...	...	...
2	15	473.357290231	...	...	...

Table 9: Results of the three optimizations for a reference star with a two-transition core and assuming different levels of precision: current fit, ground-based data and *Kepler* data precision.

	Test case 1	Test case 2	Test case 3
	$\mu = 0 \ \sigma = 10 \ \mu\text{Hz}$	$\mu = 0 \ \sigma = 0.1 \ \mu\text{Hz}$	$\mu = 0 \ \sigma = 0.001 \ \mu\text{Hz}$
$S^2$	2.8	$2.7 \times 10^{-4}$	$2.9 \times 10^{-8}$
$< \Delta\nu > (\mu\text{Hz})$	5.41	0.061	0.00072
$< \Delta X/X > (\%)$	0.14	$1.50 \times 10^{-3}$	$1.60 \times 10^{-5}$
$T_{\text{eff}} (\text{K})$	$11880 \pm 90$ ( 1 %)	$11999.0 \pm 1.5$ ( 0.008 %)	$11999.98 \pm 0.05$ ( 0.0002%)
$\text{Log } g$	$8.037 \pm 0.020$ ( 0.5 %)	$8.00052 \pm 0.00015$ ( 0.007 %)	$8.000005 \pm 0.000013$ ( 0.001%)
$D(\text{H})$	$-5.15 \pm 0.08$ ( 3 %)	$-5.002 \pm 0.0012$ ( 0.04 %)	$-5.00002 \pm 0.00004$ ( 0.0004%)
$D(\text{He})$	$-3.15 \pm 0.06$ ( 5 %)	$-3.002 \pm 0.001$ ( 0.07 %)	$-3.00005 \pm 0.00003$ ( 0.002 %)
Total mass ( $M_{\odot}$ )	$0.62 \pm 0.01$ ( 4 %)	$0.5955 \pm 0.0002$ ( 0.05 %)	$0.595209 \pm 0.000006$ ( 0.0002 %)
Radius ( $R_{\odot}$ )	$0.0124 \pm 0.0002$ ( 3 %)	$0.012765 \pm 0.000002$ ( 0.04 %)	$0.0127698 \pm 0.0000001$ ( 0.002%)
Core oxygen fraction (%)	$70 \pm 5$ ( 1 %)	$70.0 \pm 0.1$ ( 0.1 %)	$70.005 \pm 0.002$ ( 0.007 %)
$t_1$	$-0.310 \pm 0.013$ ( 3 %)	$-0.3004 \pm 0.0003$ ( 0.1 %)	$-0.29989 \pm 0.00001$ ( 0.04 %)
$\Delta t_1$	$0.044 \pm 0.023$ ( 27 %)	$0.0607 \pm 0.0010$ ( 1.2 %)	$0.05956 \pm 0.00004$ ( 0.07 %)
$t_1$ oxygen (%)	$45 \pm 5$ ( 13 %)	$40 \pm 0.2$ ( 0.3 %)	$40.038 \pm 0.003$ ( 0.1 %)
$t_2$	$-1.61 \pm 0.10$ ( 7 %)	$-1.502 \pm 0.002$ ( 0.1 %)	$-1.5009 \pm 0.0001$ ( 0.06 %)
$\Delta t_2$	$0.057 \pm 0.028$ ( 29 %)	$0.0803 \pm 0.0015$ ( 0.4 %)	$0.08008 \pm 0.00047$ ( 0.1 %)
$t_2$ oxygen (%)	$15 \pm 4$ ( 25 %)	$20.1 \pm 0.1$ ( 0.5 %)	$19.96 \pm 0.01$ ( 0.2 %)

Table 10: Parameters of the reference star and search range for the optimization using a two-transition core with the presence of the evolutionary predicted triple transition of helium, carbon and oxygen.

Parameter	Value	Search range
$T_{\text{eff}}$ (K)	12,000	11,000 - 13,000
$\text{Log } g$	8.00	7.80 - 8.20
$D(\text{H})$	−4.2	−9.0 - −4.0
$D(\text{He})$	−1.8	−4.0 - −1.5
Total mass ( $M_{\odot}$ )	$6.0541 \times 10^{-1}$	...
Radius ( $R_{\odot}$ )	$1.2879 \times 10^{-2}$	...
Core oxygen fraction (%)	72	0 - 100
$t_1$	−0.5	−0.80 - −0.15
$\Delta t_1$	0.2	0.010 - 0.30
$t_1$ oxygen (%)	40	0 - 100
$t_2$	−1.6	−2.00 - −0.60
$\Delta t_2$	0.25	0.010 - 0.30
$t_2$ oxygen (%)	40	0 - 100

Table 11: Selected and modified periods for the reference star with the two-transition core with the presence of the evolutionary predicted triple transition of helium, carbon and oxygen.

$\ell$	$k$	Period (s)	$\sigma = 0.001 \mu\text{Hz}$
<b>1</b>	<b>1</b>	<b>120.452983850</b>	<b>120.45298857</b>
<b>1</b>	<b>2</b>	<b>189.003923848</b>	<b>189.00386827</b>
<b>1</b>	<b>3</b>	<b>251.065310769</b>	<b>251.06532894</b>
<b>1</b>	<b>4</b>	<b>288.146522125</b>	<b>288.14660990</b>
<b>1</b>	<b>5</b>	<b>308.669247080</b>	<b>308.66909922</b>
1	6	362.527251742	...
1	7	407.584693069	...
1	8	465.047565605	...
1	9	495.871289508	...
<b>2</b>	<b>2</b>	<b>111.787448206</b>	<b>111.78744565</b>
<b>2</b>	<b>3</b>	<b>145.458275720</b>	<b>145.45825951</b>
<b>2</b>	<b>4</b>	<b>168.756963139</b>	<b>168.75696163</b>
<b>2</b>	<b>5</b>	<b>200.954894937</b>	<b>200.95494249</b>
<b>2</b>	<b>6</b>	<b>211.835583311</b>	<b>211.83557666</b>
2	7	236.460839397	...
2	8	270.690939915	...
2	9	294.553272794	...
2	10	320.151012113	...
2	11	341.454056864	...
2	12	364.828511100	...
2	13	383.707614573	...
2	14	406.414434402	...
2	15	434.387667041	...
2	16	456.565643881	...
2	17	478.331486497	...

Table 12: Results of the optimization for a reference star with a two-transition core with the presence of the evolutionary predicted triple transition of helium, carbon and oxygen and assuming *Kepler* data precision.

Test case 3	
$\mu = 0 \ \sigma = 0.001 \ \mu\text{Hz}$	
$S^2$	$4.0 \times 10^{-9}$
$\langle \Delta\nu \rangle \ (\mu\text{Hz})$	0.001
$\langle \Delta X/X \rangle \ (\%)$	$1.6 \times 10^{-5}$
$T_{\text{eff}} \ (\text{K})$	$11,999.69 \pm 0.02 \ (0.003 \ \%)$
$\text{Log } g$	$8.000028 \pm 0.000003 \ (0.0004 \ \%)$
$D(\text{H})$	$-4.20008 \pm 0.00001 \ (0.002 \ \%)$
$D(\text{He})$	$-1.80005 \pm 0.00001 \ (0.003 \ \%)$
Total mass ( $M_{\odot}$ )	$0.605420 \pm 0.000001 \ (0.002 \ \%)$
Radius ( $R_{\odot}$ )	$0.01287854 \pm 0.00000003 \ (0.002 \ \%)$
Core oxygen fraction (%)	$72.0325 \pm 0.0001 \ (0.05 \ \%)$
$t_1$	$-0.499775 \pm 0.000002 \ (0.05 \ \%)$
$\Delta t_1$	$0.19972 \pm 0.00001 \ (0.1 \ \%)$
$t_1$ oxygen (%)	$40.0512 \pm 0.0005 \ (0.1 \ \%)$
$t_2$	$-1.60010 \pm 0.00002 \ (0.06 \ \%)$
$\Delta t_2$	$0.2497 \pm 0.0001 \ (0.1 \ \%)$
$t_2$ oxygen (%)	$39.999 \pm 0.003 \ (0.003 \ \%)$

Table 13: Pulsation spectra for the five test cases.

Case 1	Case 2	Case 3	Case 4	Case 5
109 s	128 s	111 s	118 s	113 s
125 s	173 s	113 s	148 s	143 s
148 s	179 s	136 s	199 s	193 s
228 s	183 s	146 s	207 s	234 s
282 s	196 s	281 s	362 s	247 s
285 s	209 s	283 s	363 s	301 s
329 s	236 s	323 s	367 s	326 s
374 s	377 s	338 s	389 s	367 s
400 s	388 s	399 s	430 s	450 s
423 s	486 s	490 s	455 s	460 s

Table 14: Global fit properties obtained for each random period sequence and each core parametrization.

	Case 1	Case 2	Case 3	Case 4	Case 5	Mean	Median
Hom. core:	$S^2 = 23.9$	$S^2 = 209.0$	$S^2 = 212.0$	$S^2 = 57.6$	$S^2 = 15.2$	103.5	57.6
	$\langle \Delta\nu \rangle = 35.1 \mu\text{Hz}$	$\langle \Delta\nu \rangle = 90.6 \mu\text{Hz}$	$\langle \Delta\nu \rangle = 159.1 \mu\text{Hz}$	$\langle \Delta\nu \rangle = 41.6 \mu\text{Hz}$	$\langle \Delta\nu \rangle = 16.1 \mu\text{Hz}$	68.5	41.6
	$\langle \Delta P \rangle = 1.6 \text{ s}$	$\langle \Delta P \rangle = 3.8 \text{ s}$	$\langle \Delta P \rangle = 3.9 \text{ s}$	$\langle \Delta P \rangle = 2.0 \text{ s}$	$\langle \Delta P \rangle = 0.9 \text{ s}$	2.44	2.0
1 transition:	$S^2 = 11.3$	$S^2 = 22.0$	$S^2 = 4.0$	$S^2 = 31.1$	$S^2 = 6.6$	15.0	11.3
	$\langle \Delta\nu \rangle = 10.5 \mu\text{Hz}$	$\langle \Delta\nu \rangle = 34.2 \mu\text{Hz}$	$\langle \Delta\nu \rangle = 12.7 \mu\text{Hz}$	$\langle \Delta\nu \rangle = 17.8 \mu\text{Hz}$	$\langle \Delta\nu \rangle = 7.6 \mu\text{Hz}$	16.6	12.7
	$\langle \Delta P \rangle = 0.7 \text{ s}$	$\langle \Delta P \rangle = 1.2 \text{ s}$	$\langle \Delta P \rangle = 0.5 \text{ s}$	$\langle \Delta P \rangle = 1.3 \text{ s}$	$\langle \Delta P \rangle = 0.6 \text{ s}$	0.9	0.7
2 transitions:	$S^2 = 6.6$	$S^2 = 9.0$	$S^2 = 1.9$	$S^2 = 10.3$	$S^2 = 3.7$	6.3	6.6
	$\langle \Delta\nu \rangle = 21.6 \mu\text{Hz}$	$\langle \Delta\nu \rangle = 18.0 \mu\text{Hz}$	$\langle \Delta\nu \rangle = 12.0 \mu\text{Hz}$	$\langle \Delta\nu \rangle = 10.9 \mu\text{Hz}$	$\langle \Delta\nu \rangle = 13.0 \mu\text{Hz}$	15.1	13.0
	$\langle \Delta P \rangle = 0.5 \text{ s}$	$\langle \Delta P \rangle = 0.7 \text{ s}$	$\langle \Delta P \rangle = 0.3 \text{ s}$	$\langle \Delta P \rangle = 0.9 \text{ s}$	$\langle \Delta P \rangle = 0.5 \text{ s}$	0.6	0.5

Table 15: Parameters of the reference model.

Parameter	Value	Search range
$T_{\text{eff}}$ (K)	12,000	11,000 - 13,000
$\text{Log } g$	8.00	7.80 - 8.20
$q(\text{H})$	-4.04	$[D(\text{H})]$ -9.0 - -4.0
$q(\text{He})$	-2.10	$[D(\text{He})]$ -4.0 - -1.5



Table 16: Periods from the reference model and from the resulting optimizations.

$\ell$	$k$	Chosen periods (s)	$\ell$	$k$	Var. hom. core (s)	$\ell$	$k$	1-transition (s)	$\ell$	$k$	2-transition (s)
1	2	206.429533263	2	5	207.80387574	1	2	205.91667143	1	2	206.30355349
1	3	259.558241480	1	3	261.26271139	1	3	260.35665876	1	3	259.72976629
1	4	285.787098098	2	9	285.94654263	1	4	285.73410324	1	4	285.88885831
1	5	316.227894252	2	10	315.89655226	1	5	314.83482318	1	5	316.31323695
1	6	375.973051700	1	6	373.22825616	1	6	375.51411398	2	12	376.01101225
2	3	150.725138295	2	3	151.01496289	2	3	150.89406262	2	3	150.78465417
2	4	177.098921306	2	4	178.19931882	2	4	178.35162669	2	4	177.05147091
2	5	195.326732918	1	2	196.91534658	2	5	195.37498858	2	5	195.34102115
2	6	218.924655751	2	6	217.81162674	2	6	217.73166428	2	6	218.75794933
2	7	245.287135903	2	7	245.41225685	2	7	247.37133055	2	7	245.34295988

Table 17: Retrieved stellar parameters from the three optimizations.

Parameter	Var. hom. core	1-transition	2-transition
$S^2$	17.5	10.4	$1.0 \times 10^{-1}$
$\langle \Delta\nu \rangle$ ( $\mu\text{Hz}$ )	19.6	15.0	1.7
$\langle \Delta P \rangle$ (s)	1.1	0.8	0.09
$T_{\text{eff}}$ (K)	12,820 (6.8%)	12,540 (4.5%)	11,770 (1.9%)
$\text{Log } g$	8.11 (1.4%)	8.04 (0.5%)	8.02 (0.3%)
$q(\text{H})$	−4.60 (13.9%)	−4.35 (7.7%)	−4.15 (2.7%)
$q(\text{He})$	−2.53 (20.5%)	−2.25 (7.1%)	−2.35 (11.9%)

## FIGURE CAPTIONS

Fig. 1 — Proposed parametrization of  $X(\text{O})$  using a two-transition model white dwarf core. All the parameters are labeled in the schematic view shown in left panel. As illustrated in right panel, the parametrization defines control points (red dots) through which the profile is interpolated using Akima splines (the thick blue curve). Other interpolation schemes are possible, e.g., linear (thin curve) or cubic splines (dotted curve), but either lead to less smooth or less stable profiles.

Fig. 2 — Calculated helium profiles extracted from a representative evolutionary sequence that includes diffusion (black solid curves) with corresponding  $M_* = 0.6 M_\odot$ ,  $\log M(\text{He})/M_* = -3.0$  and  $\log M(\text{H})/M_* = -5.0$ , at three different effective temperatures around 30,000K (top panel), 20,000K (middle panel) and 12,000K (bottom panel), compared to static parametrized models (red dotted curves) obtained with optimized values of  $Pf_{\text{H}}$  and  $Pf_{\text{He}}$ .

Fig. 3 — Top panel: Chemical abundance profiles of a generic model using our two-transition model white dwarf core mimicking the general structures of a typical model of a DA white dwarf star (left panel) taken from evolutionary calculations connecting with the ZAMS (from Althaus et al. 2010, Figure 6), and of a typical model of a DB white dwarf star (right panel) taken as well from detailed evolutionary calculations (from Córscico et al. 2012, Figure 2). Oxygen (long-dashed curve), carbon (dashed curve), helium (dotted curve), and hydrogen (solid curve) are depicted on the Figure. The abscissa shows the fractional mass depth (with  $\log q = 0$  corresponding to the center of the star). Bottom panel: run of the square of the Brunt-Väisälä frequency (solid curves) and of the Lamb frequency for  $l = 1$  (lower dotted curve) and  $l = 2$  (upper dotted curve). The left part of both panels emphasizes a zoomed-in view of the deep interior of the star.

Fig. 4 — Map of the projected merit function  $S^2$  (on a log scale) onto the  $T_{\text{eff}}\text{-}\log g$  and  $D(\text{He})\text{-}D(\text{H})$  plane as well as the probability density functions for all the retrieved stellar parameters from the reference star with a variable homogeneous core. The degree of precision of the “observations” is set to the current fit precision level. The red-hatched region between two vertical solid red lines defines the  $1\sigma$  range, containing 68.3% of the distribution. The blue vertical dashed line indicates the value from the reference model.

Fig. 5 — Map of the projected merit function  $S^2$  (on a log scale) onto the  $T_{\text{eff}}\text{-}\log g$  and  $D(\text{He})\text{-}D(\text{H})$  plane as well as the probability density functions for all the retrieved stellar parameters from the reference star with a variable homogeneous core. The degree of precision of the “observations” is set to the ground-based data level. The red-hatched region between two vertical solid red lines defines the  $1\sigma$  range, containing 68.3% of the distribution. The blue vertical dashed line indicates the value from the reference model.

Fig. 6 — Map of the projected merit function  $S^2$  (on a log scale) onto the  $T_{\text{eff}}\text{-log } g$  and  $D(\text{He})\text{-}D(\text{H})$  plane as well as the probability density functions for all the retrieved stellar parameters from the reference star with a variable homogeneous core. The degree of precision of the “observations” is set to the *Kepler* data level. The red-hatched region between two vertical solid red lines defines the  $1\sigma$  range, containing 68.3% of the distribution. The blue vertical dashed line indicates the value from the reference model.

Fig. 7 — Map of the projected merit function  $S^2$  (on a log scale) onto the  $T_{\text{eff}}\text{-log } g$  and  $D(\text{He})\text{-}D(\text{H})$  plane as well as the probability density functions for all the retrieved stellar parameters from the reference star with one-transition core. The degree of precision of the “observations” is set to the current fit precision level. The red-hatched region between two vertical solid red lines defines the  $1\sigma$  range, containing 68.3% of the distribution. The blue vertical dashed line indicates the value from the reference model.

Fig. 7 — Continued.

Fig. 8 — Map of the projected merit function  $S^2$  (on a log scale) onto the  $T_{\text{eff}}\text{-log } g$  and  $D(\text{He})\text{-}D(\text{H})$  plane as well as the probability density functions for all the retrieved stellar parameters from the reference star with one-transition core. The degree of precision of the “observations” is set to the ground-based data precision level. The red-hatched region between two vertical solid red lines defines the  $1\sigma$  range, containing 68.3% of the distribution. The blue vertical dashed line indicates the value from the reference model.

Fig. 8 — Continued.

Fig. 9 — Map of the projected merit function  $S^2$  (on a log scale) onto the  $T_{\text{eff}}\text{-log } g$  and  $D(\text{He})\text{-}D(\text{H})$  plane as well as the probability density functions for all the retrieved stellar parameters from the reference star with one-transition core. The degree of precision of the “observations” is set to the *Kepler* data precision level. The red-hatched region between two vertical solid red lines defines the  $1\sigma$  range, containing 68.3% of the distribution. The blue vertical dashed line indicates the value from the reference model.

Fig. 9 — Continued.

Fig. 10 — Map of the projected merit function  $S^2$  (on a logarithmic scale) onto the  $T_{\text{eff}}\text{-log } g$  and  $D(\text{He})\text{-}D(\text{H})$  plane as well as the probability density functions for all the retrieved stellar parameters from the reference star with two-transition core. The degree of precision of the “observations” is set to the current fit precision level. The red-hatched region between two vertical solid red lines defines the  $1\sigma$  range, containing 68.3% of the distribution. The blue vertical dashed line indicates the value from the reference model.

Fig. 10 — Continued.

Fig. 11 — Map of the projected merit function  $S^2$  (on a log scale) onto the  $T_{\text{eff}}\text{-log } g$  and  $D(\text{He})\text{-}D(\text{H})$  plane as well as the probability density functions for all the retrieved stellar parameters from the reference star with two-transition core. The degree of precision of the “observations” is set to the ground-based data precision level. The red-hatched region between two vertical solid red lines defines the  $1\sigma$  range, containing 68.3% of the distribution. The blue vertical dashed line indicates the value from the reference model.

Fig. 11 — Continued.

Fig. 12 — Map of the projected merit function  $S^2$  (on a log scale) onto the  $T_{\text{eff}}\text{-log } g$  and  $D(\text{He})\text{-}D(\text{H})$  plane as well as the probability density functions for all the retrieved stellar parameters from the reference star with two-transition core. The degree of precision of the “observations” is set to the *Kepler* data precision level. The red-hatched region between two vertical solid red lines defines the  $1\sigma$  range, containing 68.3% of the distribution. The blue vertical dashed line indicates the value from the reference model.

Fig. 12 — Continued.

Fig. 13 — Top panel: Chemical abundance profiles of the reference model with a triple transition He/C/O (red curves) and the retrieved model (black curves), oxygen (long-dashed curve), carbon (dashed curve), helium (dotted curve), and hydrogen (solid curve). The abscissa shows the fractional mass depth (with  $\log q = 0$  corresponding to the center of the star). Bottom panel: run of the square of the Brunt-Väisälä frequency (solid curves) and of the Lamb frequency for  $l = 1$  (lower dotted curve) and  $l = 2$  (upper dotted curve). The left part of both panels emphasizes a zoomed-in view of the deep interior of the star.

Fig. 14 — Top panel: Chemical abundance profiles of the reference model, oxygen (long-dashed curve), carbon (dashed curve), helium (dotted curve), and hydrogen (solid curve). The abscissa shows the fractional mass depth (with  $\log q = 0$  corresponding to the center of the star). Bottom panel: run of the square of the Brunt-Väisälä frequency (solid curves) and of the Lamb frequency for  $l = 1$  (lower dotted curve) and  $l = 2$  (upper dotted curve). The left part of both panels emphasizes a zoomed-in view of the deep interior of the star.

Fig. 15 — Weight functions of the selected modes from the reference model.

Fig. 16 — Similar to Fig. 14, but showing the stratifications of the optimal model calculated with an homogeneous core (black curves) compared to those of the reference model (red curves).

Fig. 17 — Similar to Fig. 14, but showing the stratifications of the optimal model calculated with the adjustable core parametrization with one transition (black curves) compared to those of the reference model (red curves).

Fig. 18 — Similar to Fig. 14, but showing the stratifications of the optimal model calculated with the adjustable core parametrization with two transitions (black curves) compared to those of the reference model (red curves).

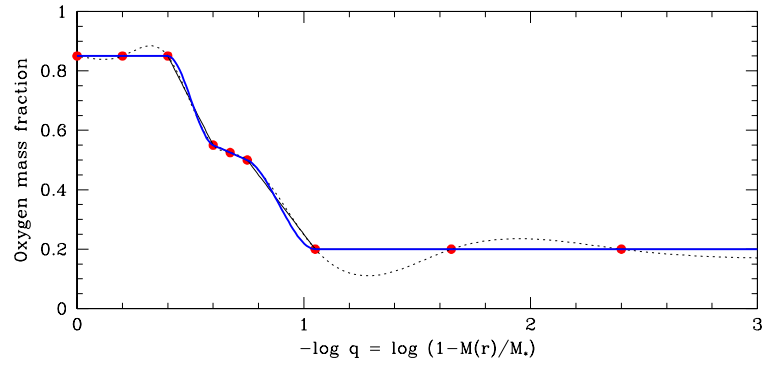
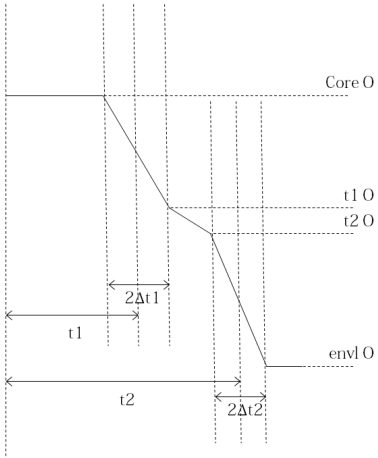


Figure 1

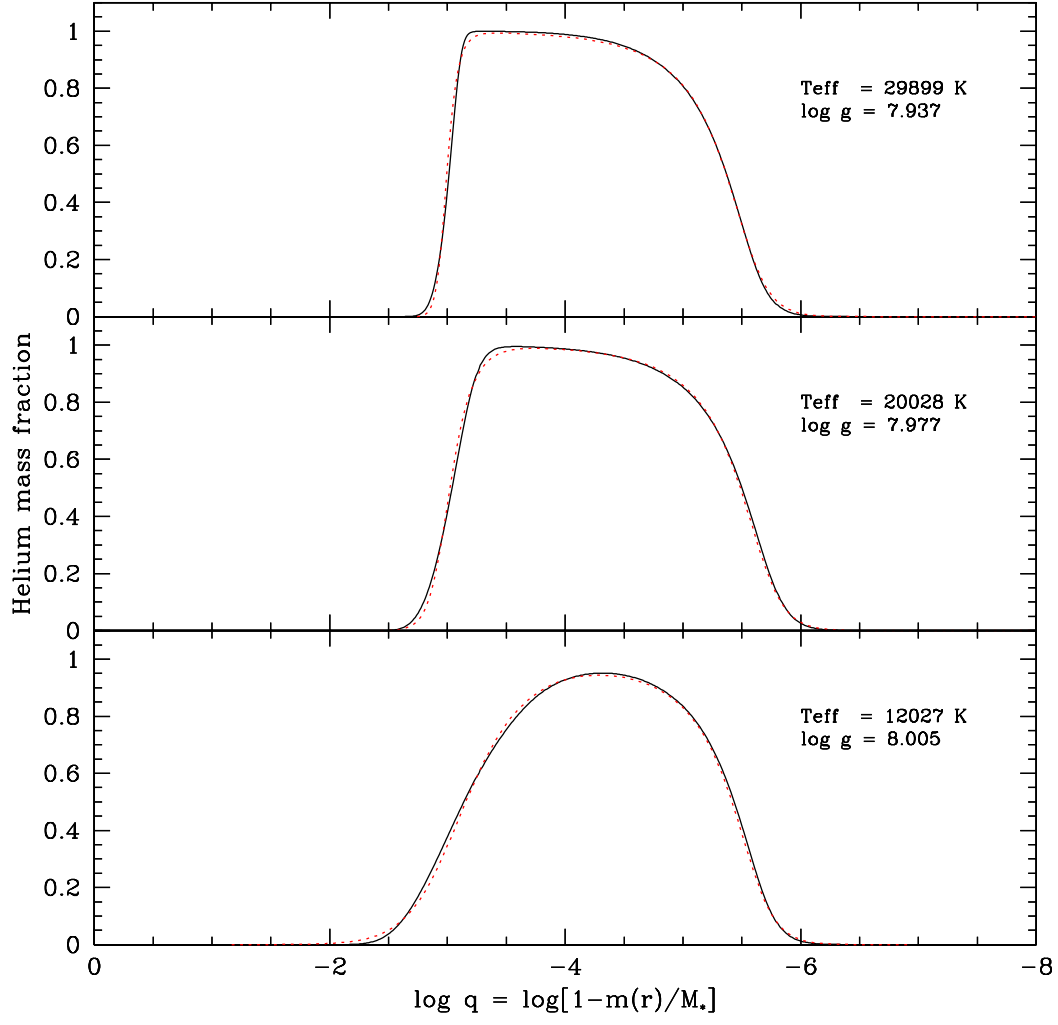


Figure 2



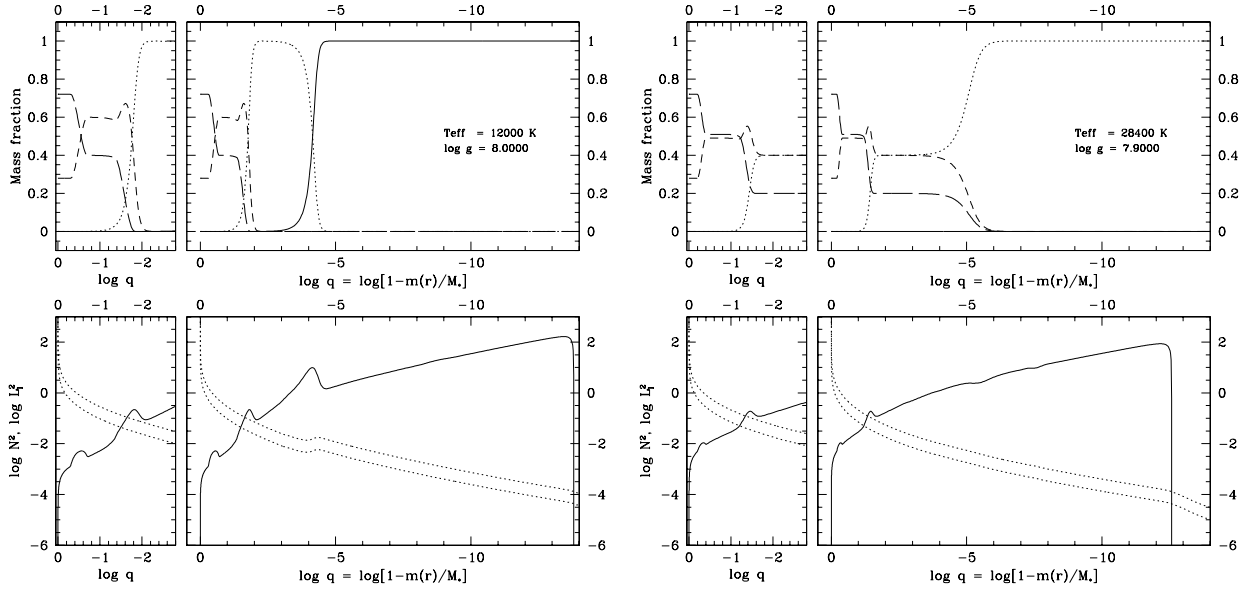


Figure 3

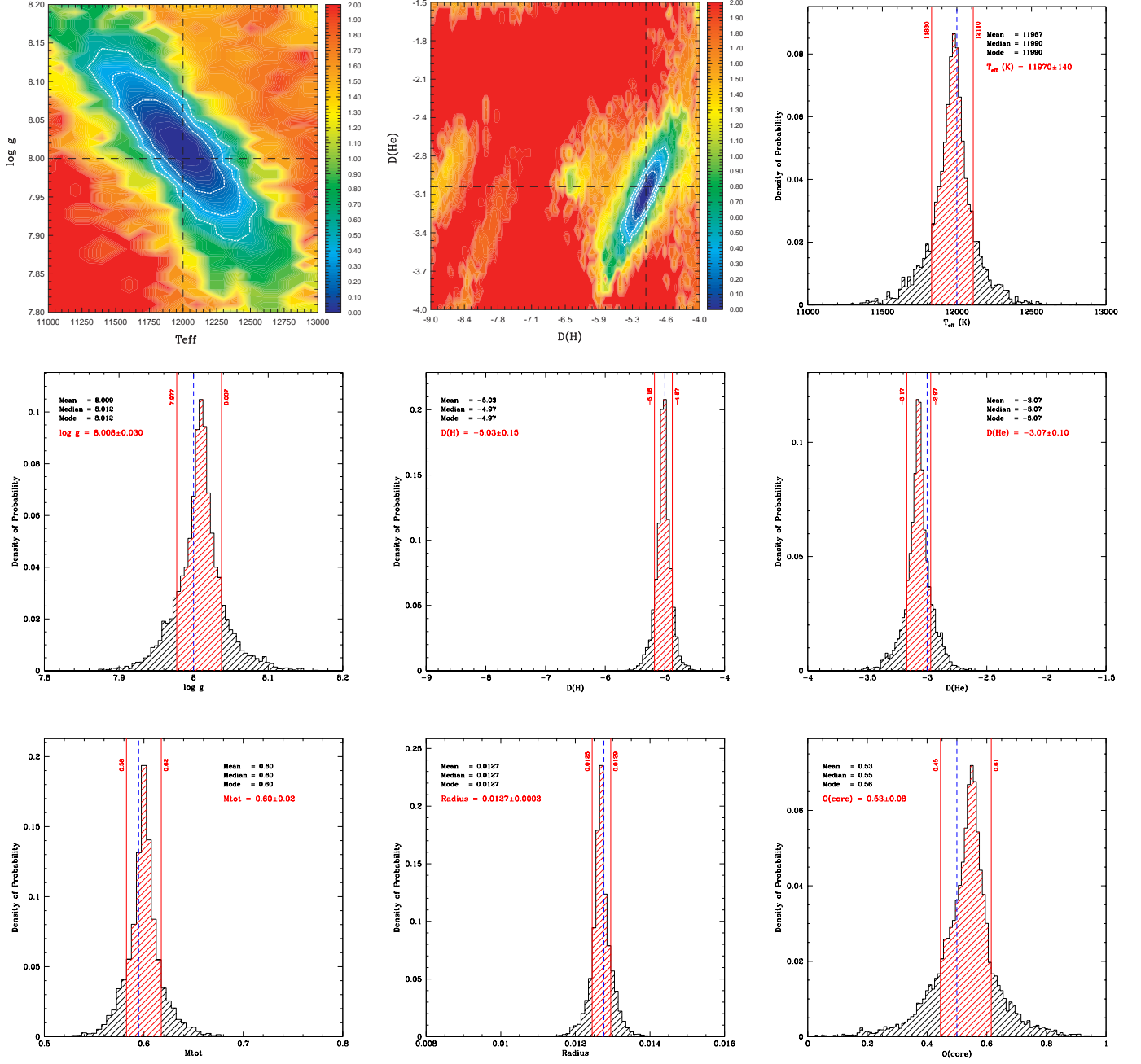


Figure 4

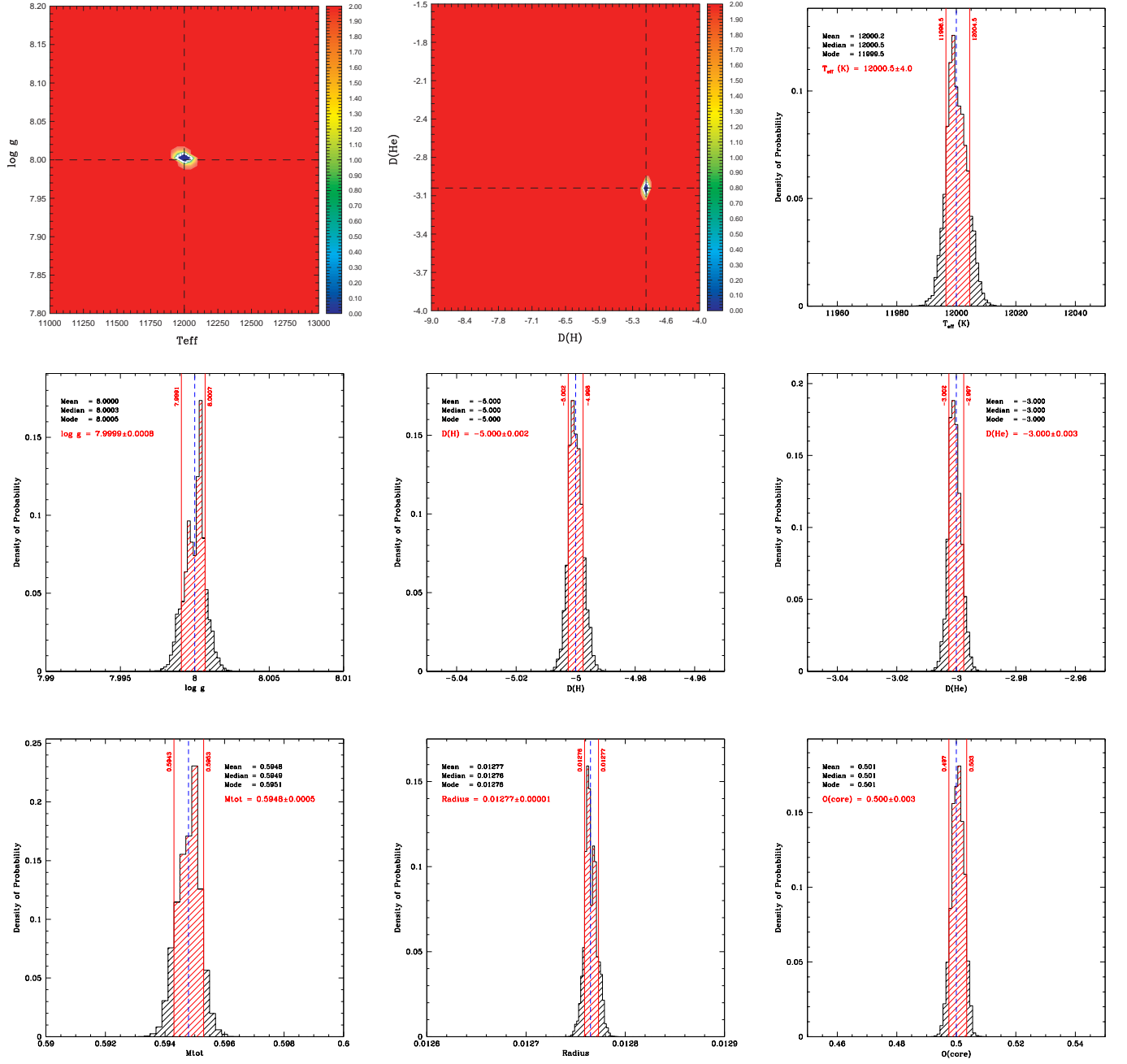


Figure 5

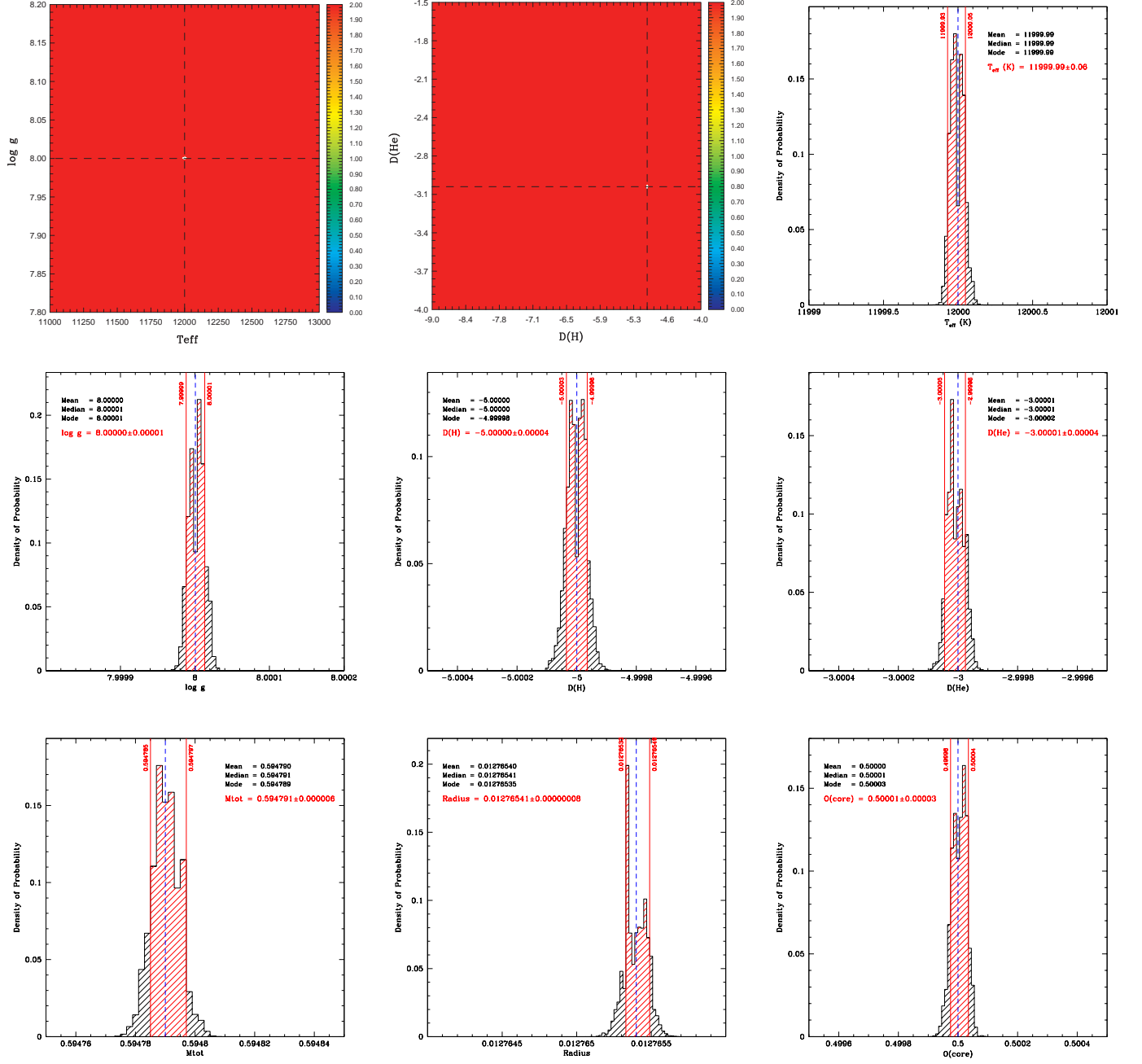


Figure 6

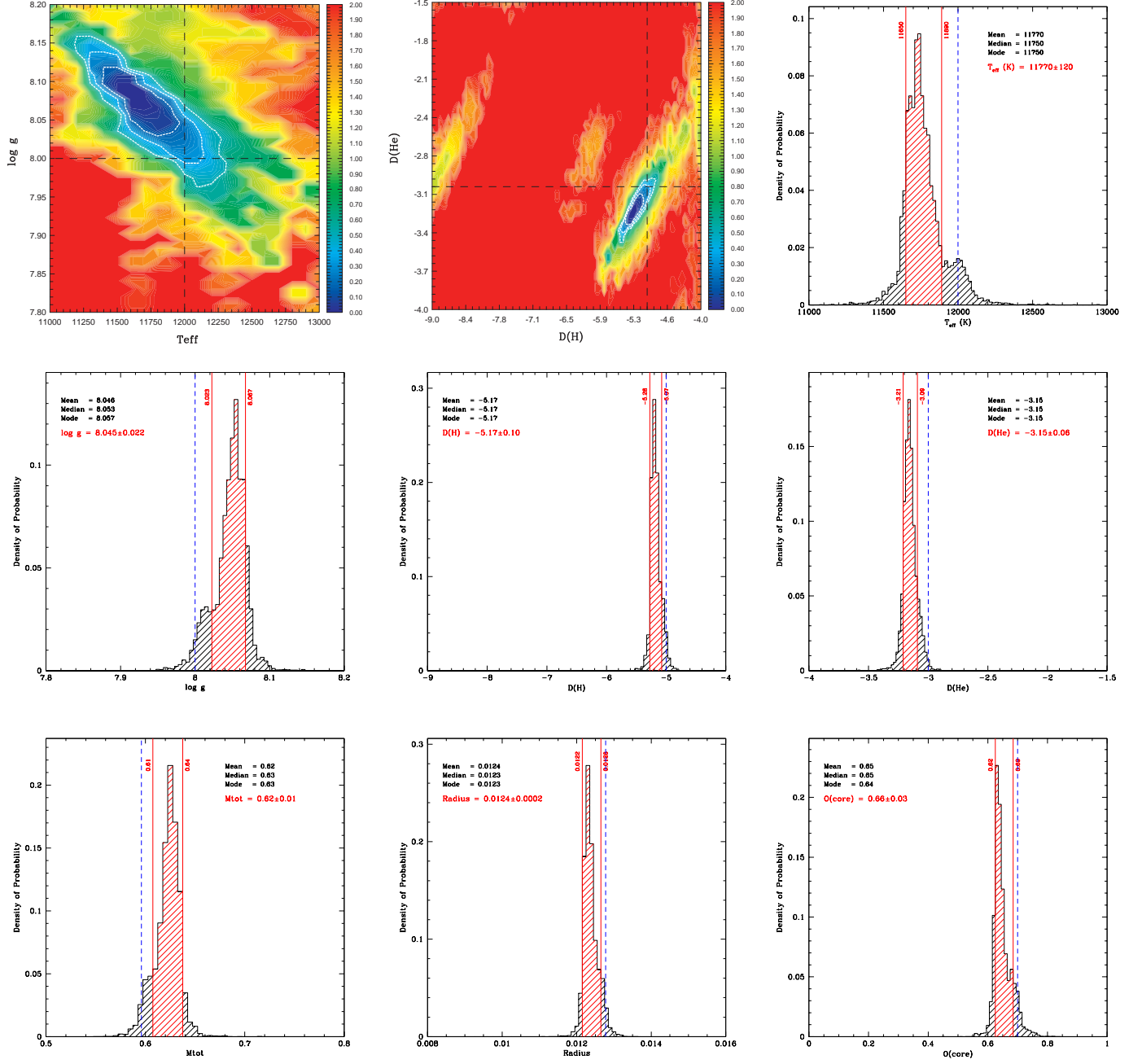


Figure 7

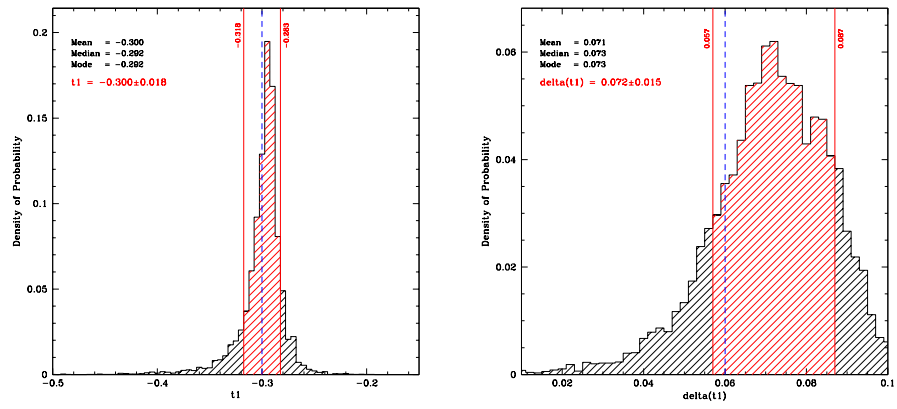


Figure 7

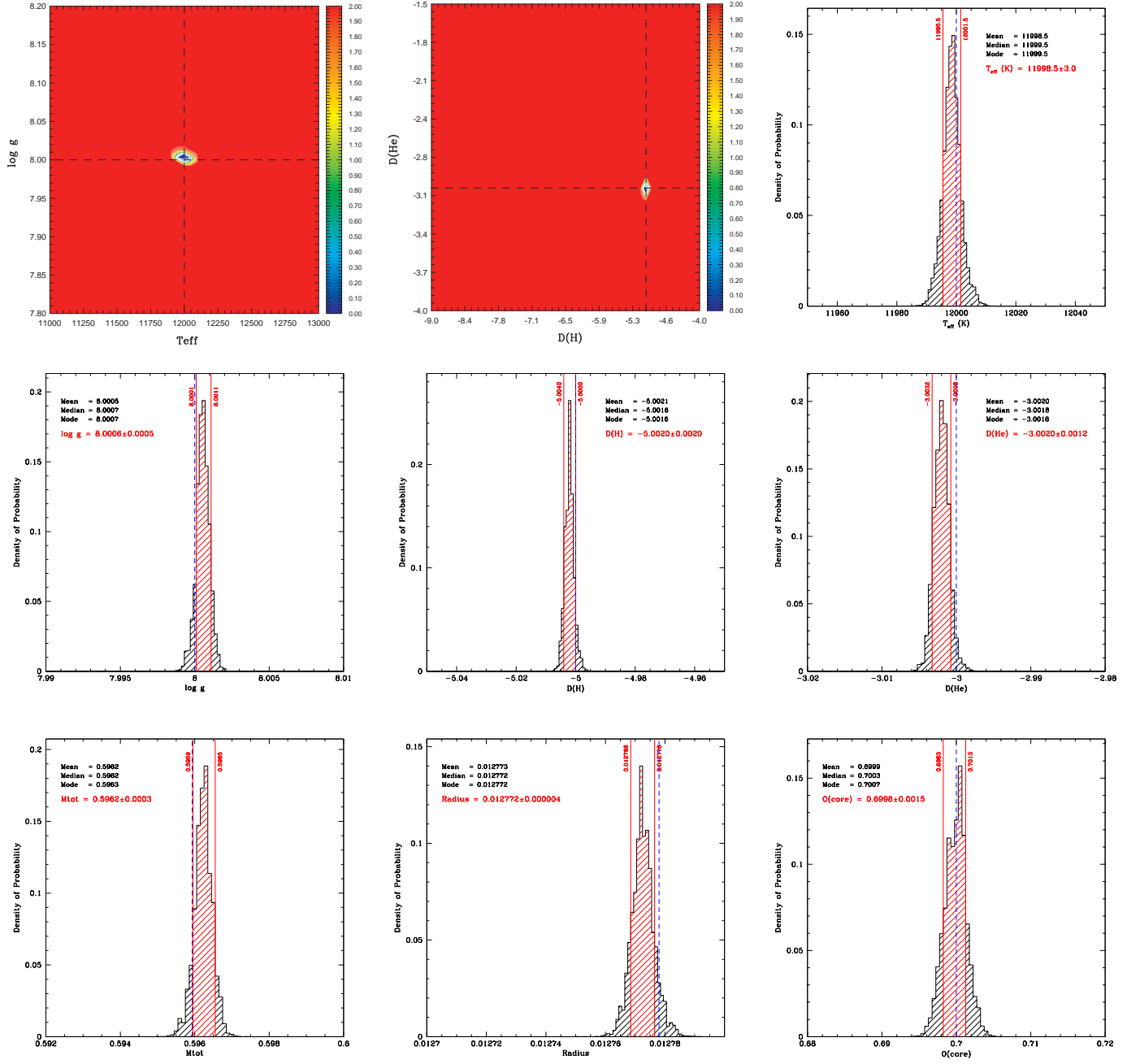


Figure 8

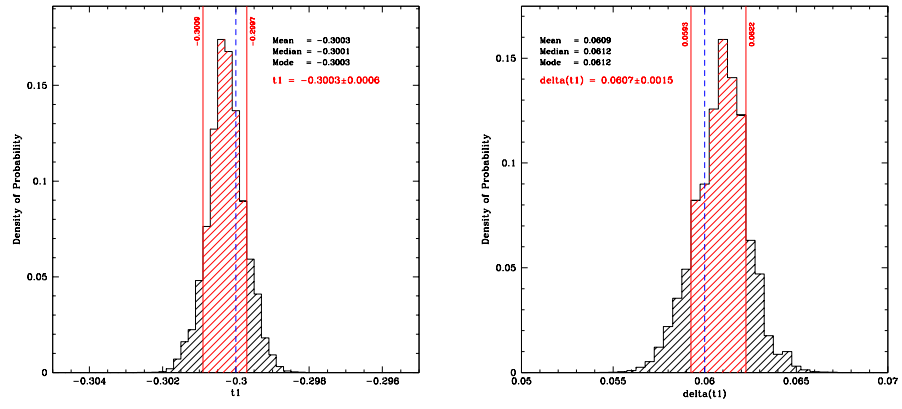


Figure 8



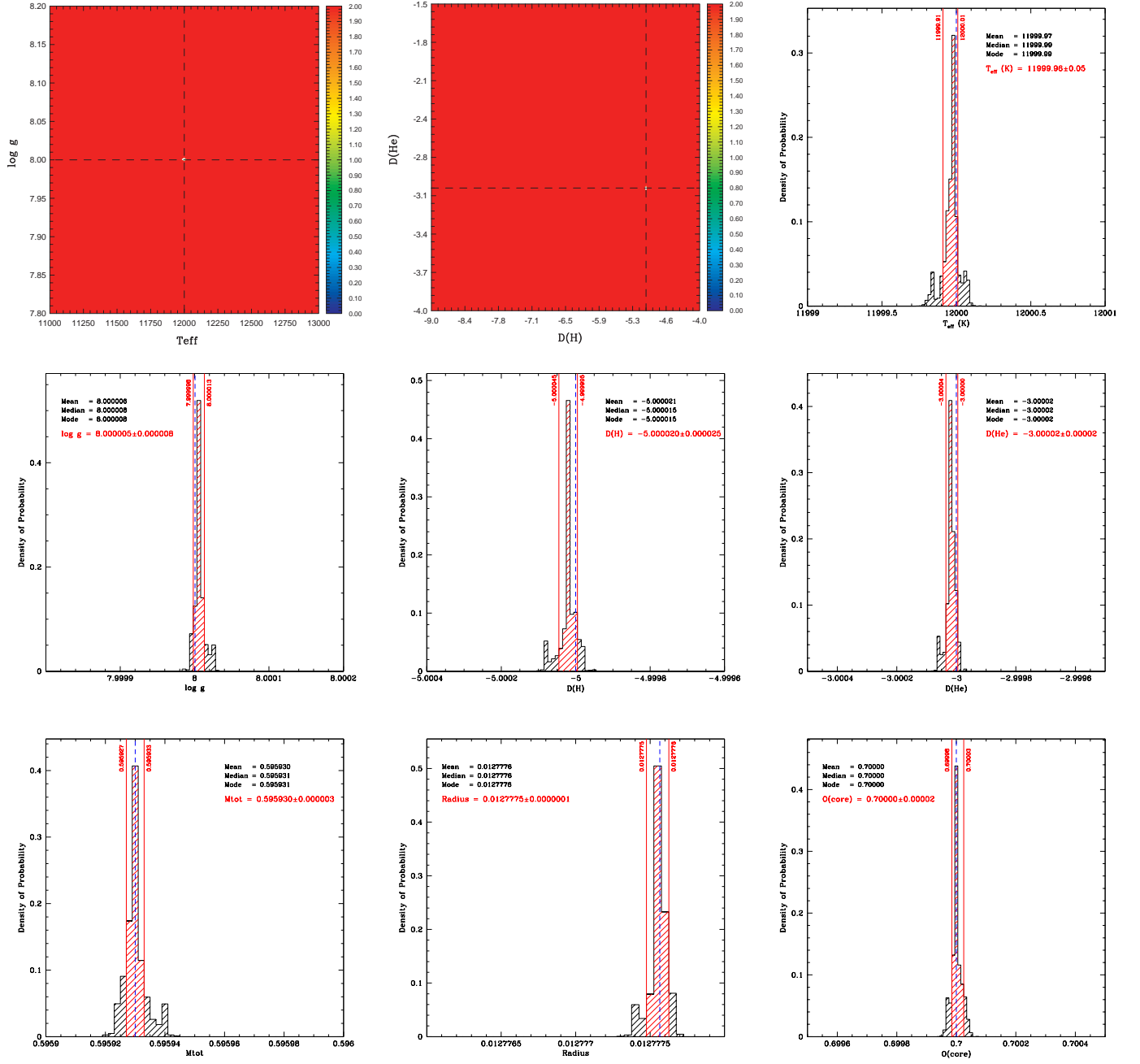


Figure 9

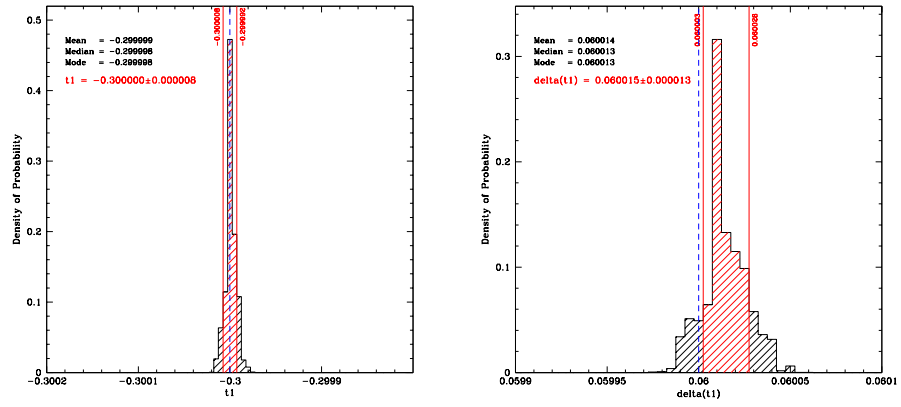


Figure 9

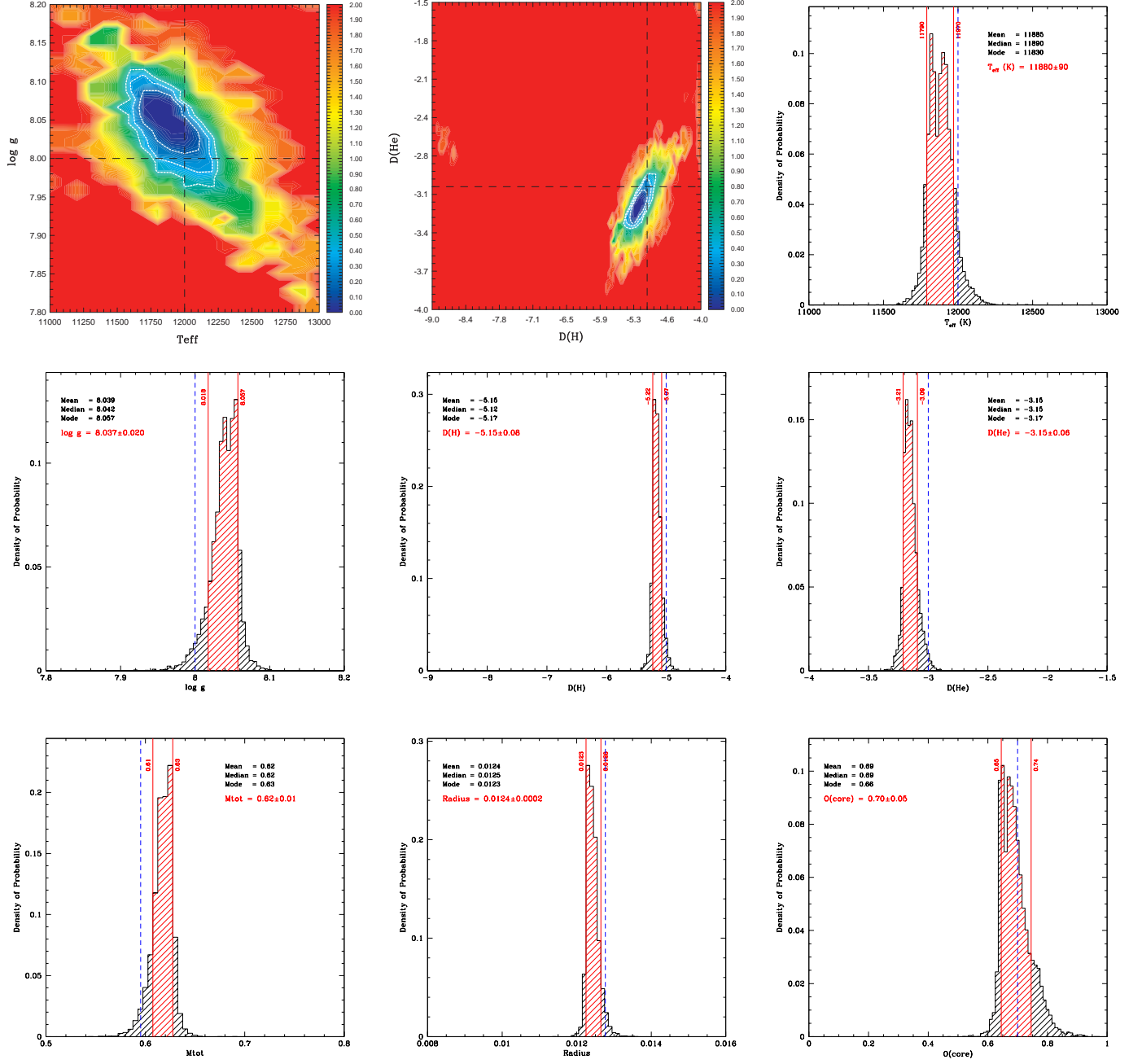


Figure 10

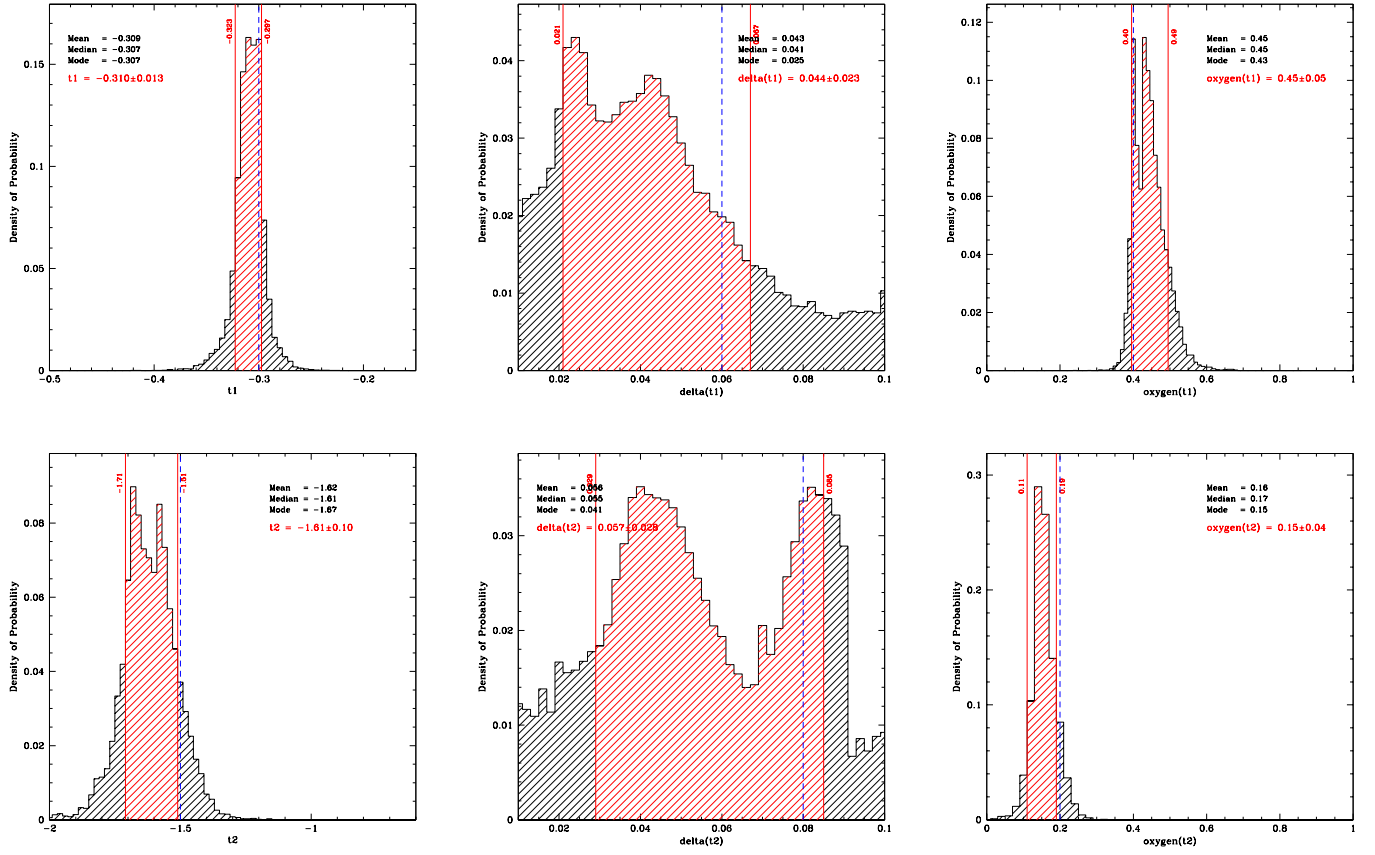


Figure 10

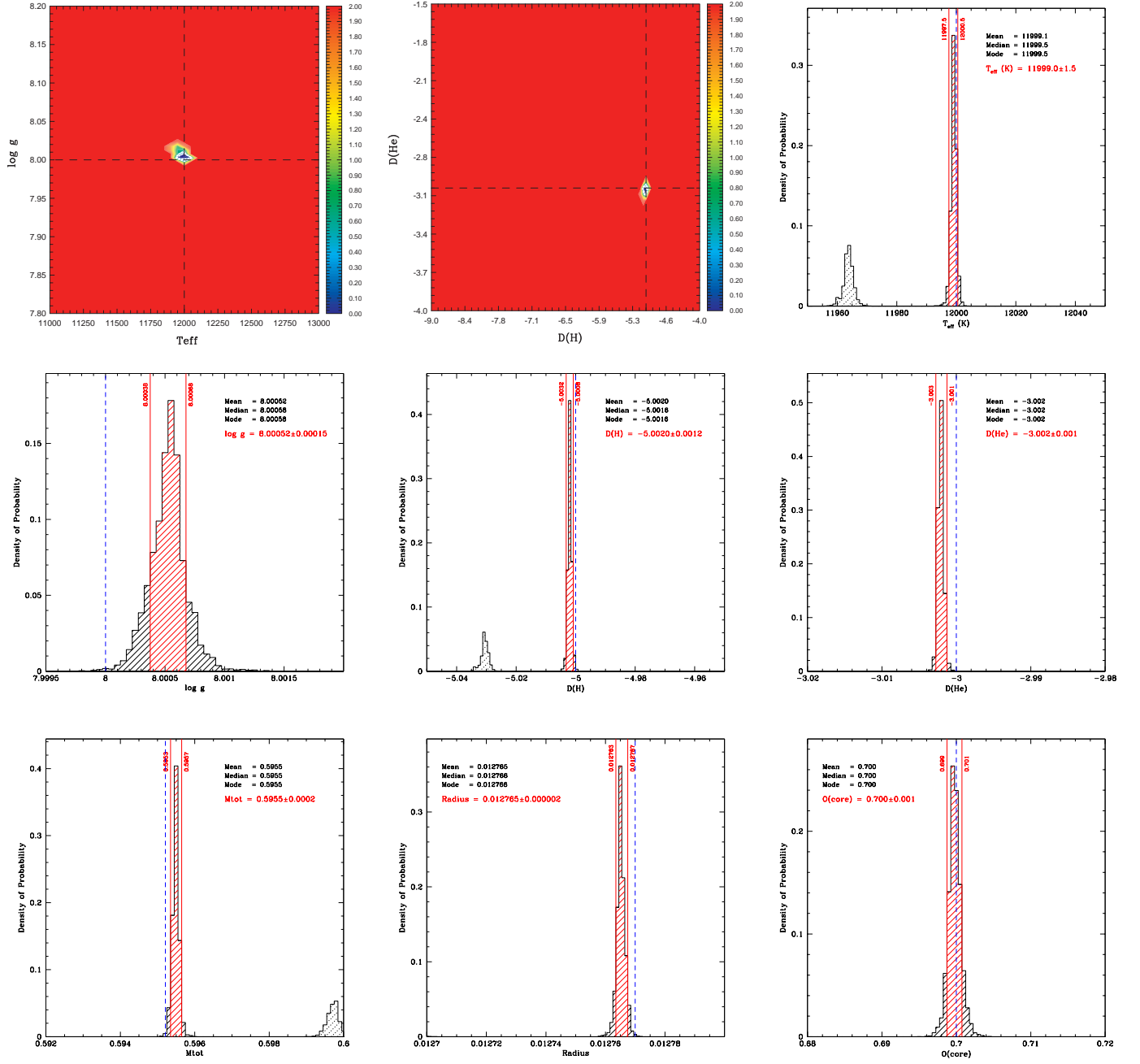


Figure 11

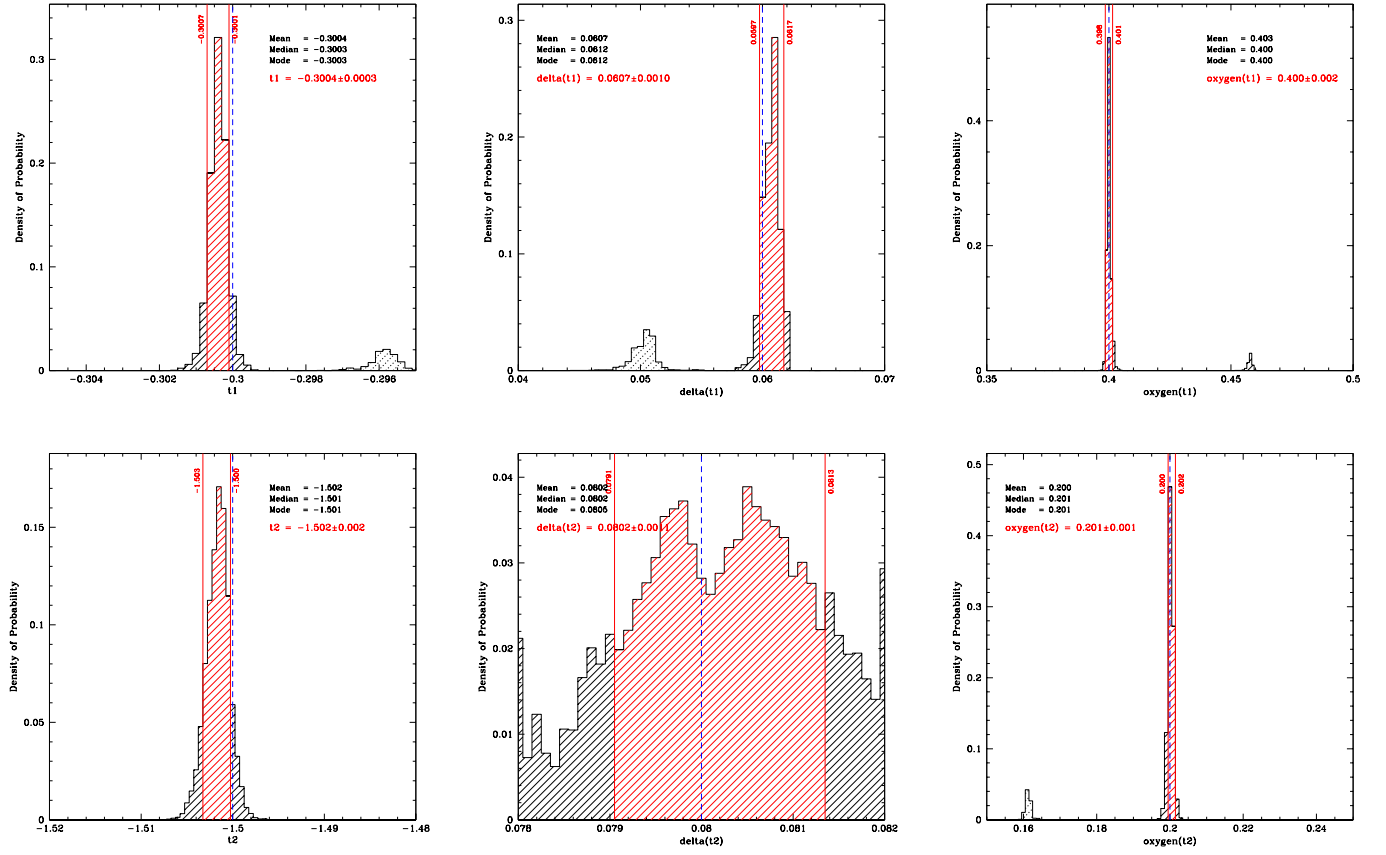


Figure 11

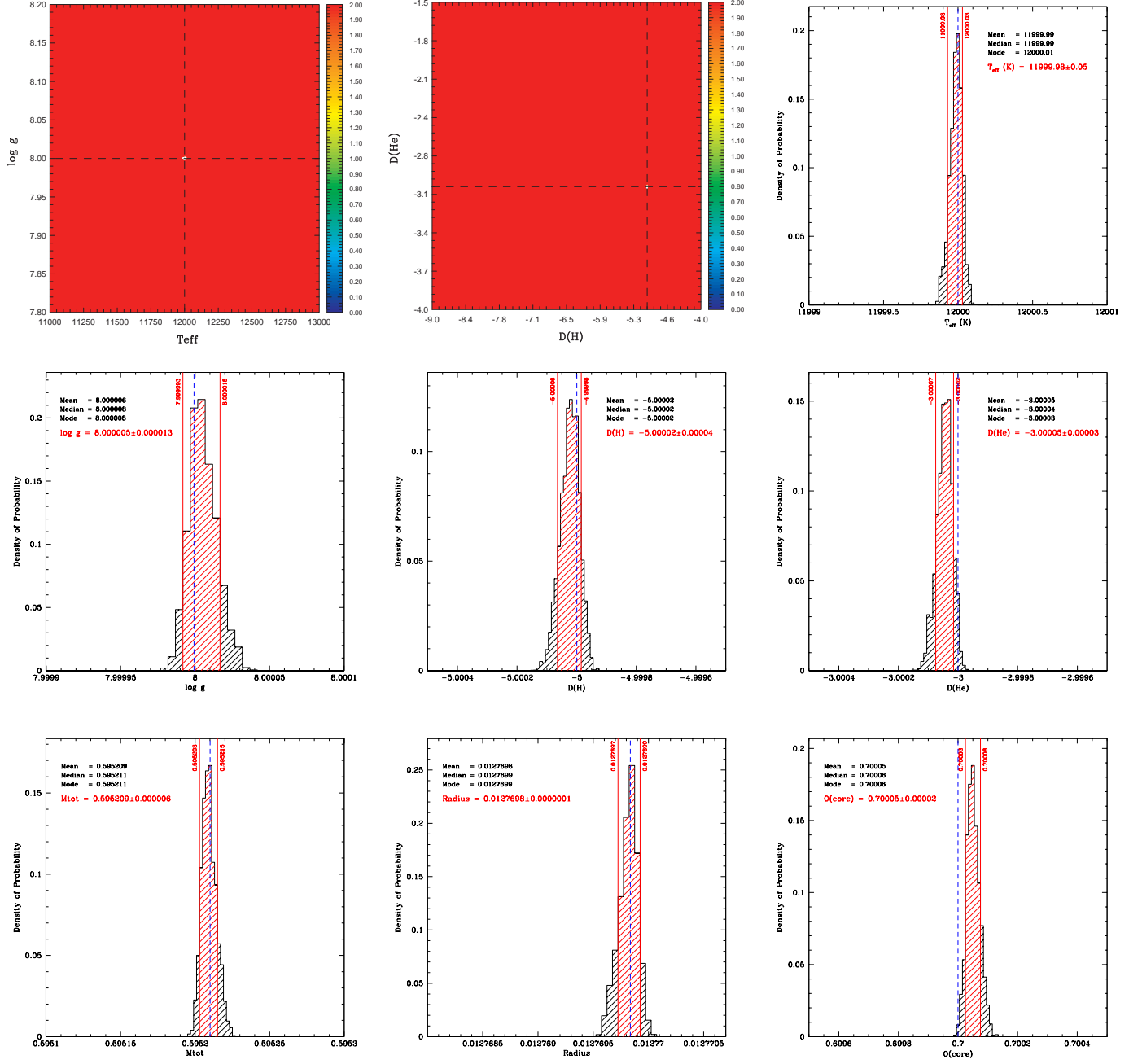


Figure 12

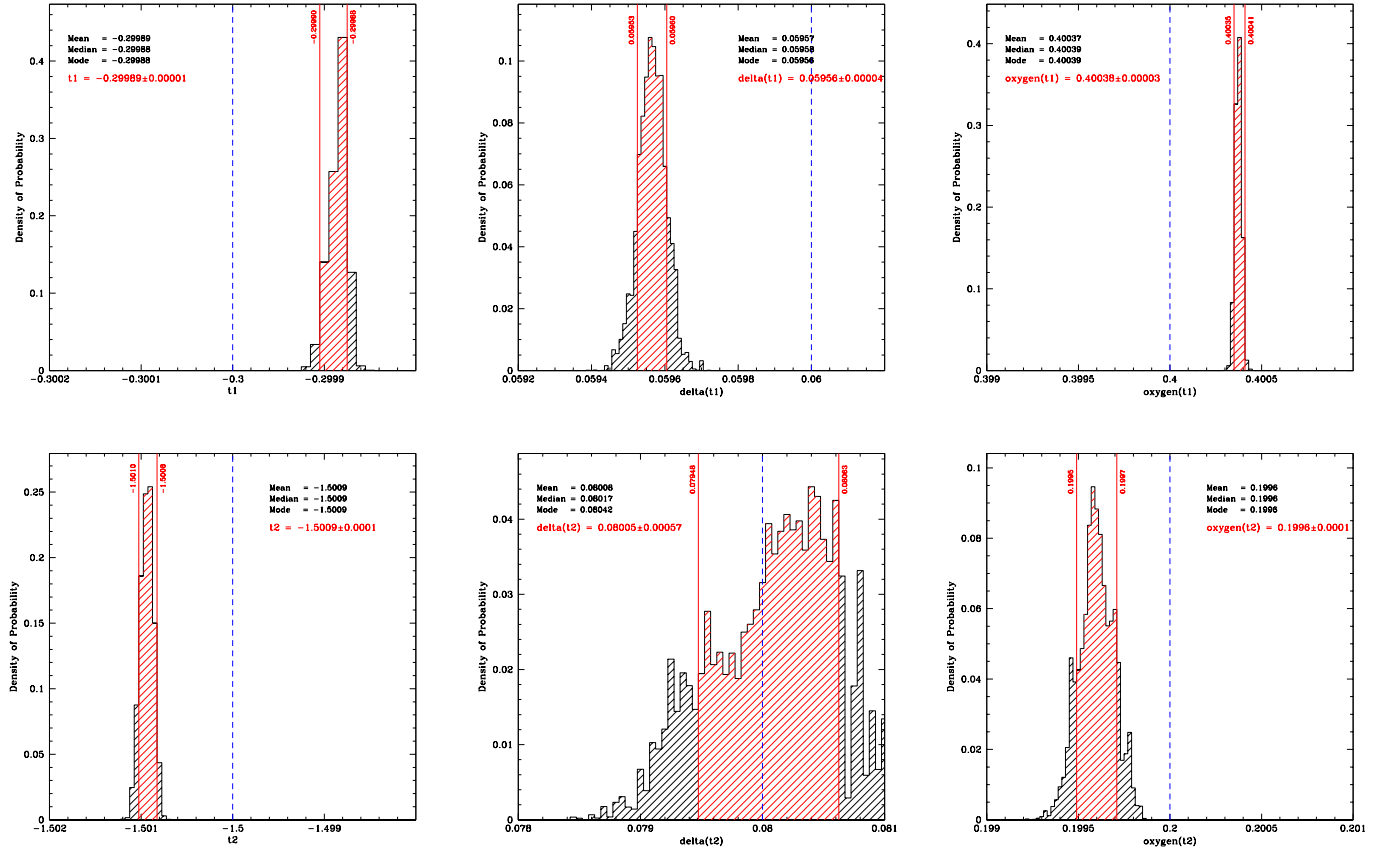


Figure 12



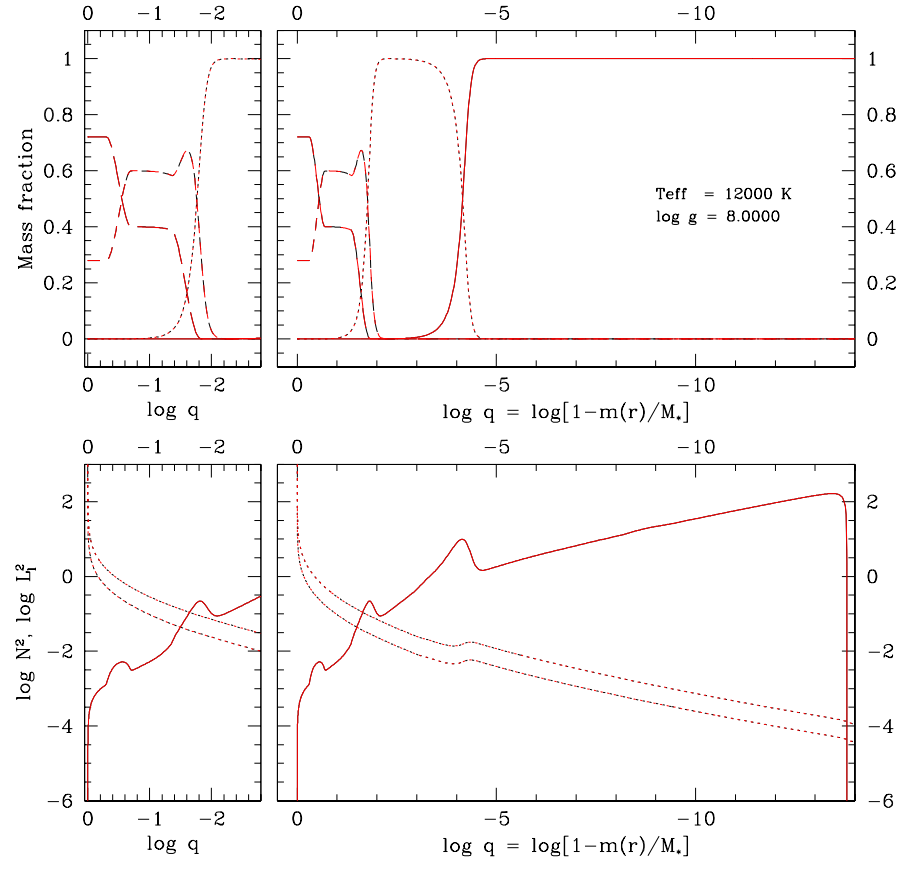


Figure 13

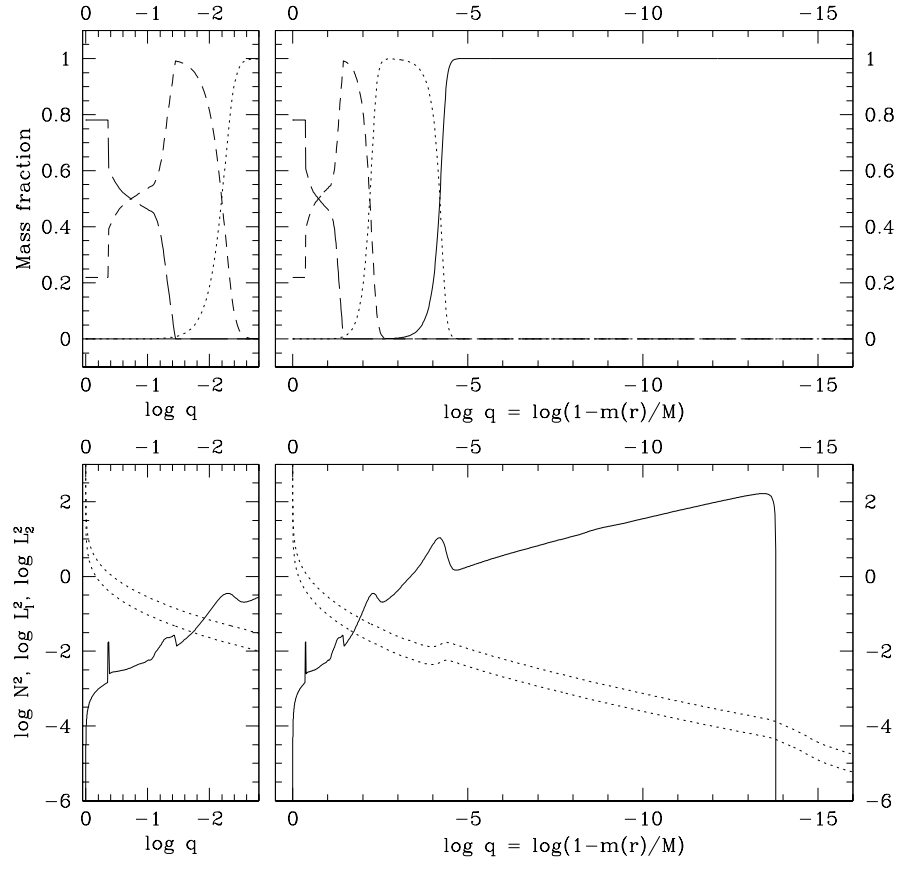


Figure 14

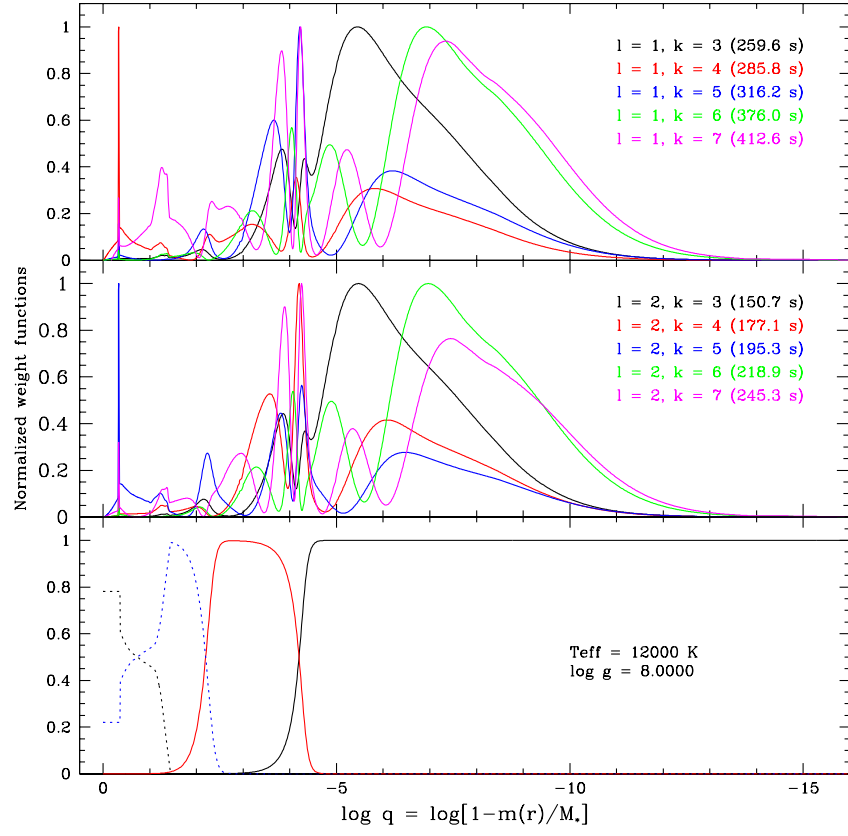


Figure 15

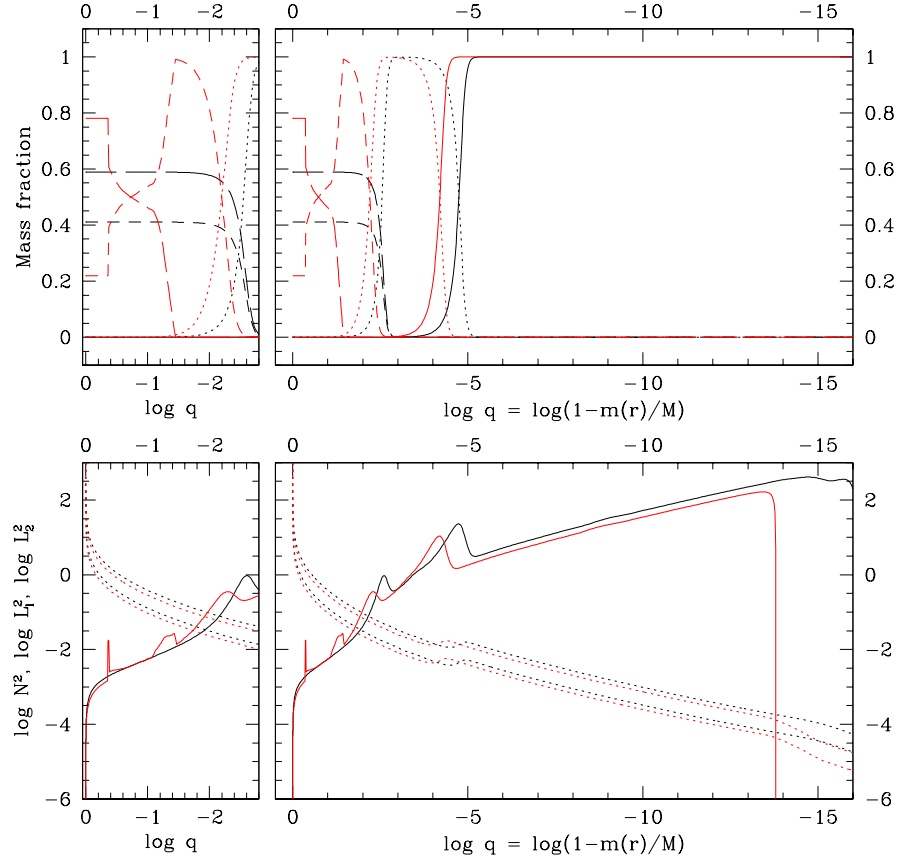


Figure 16

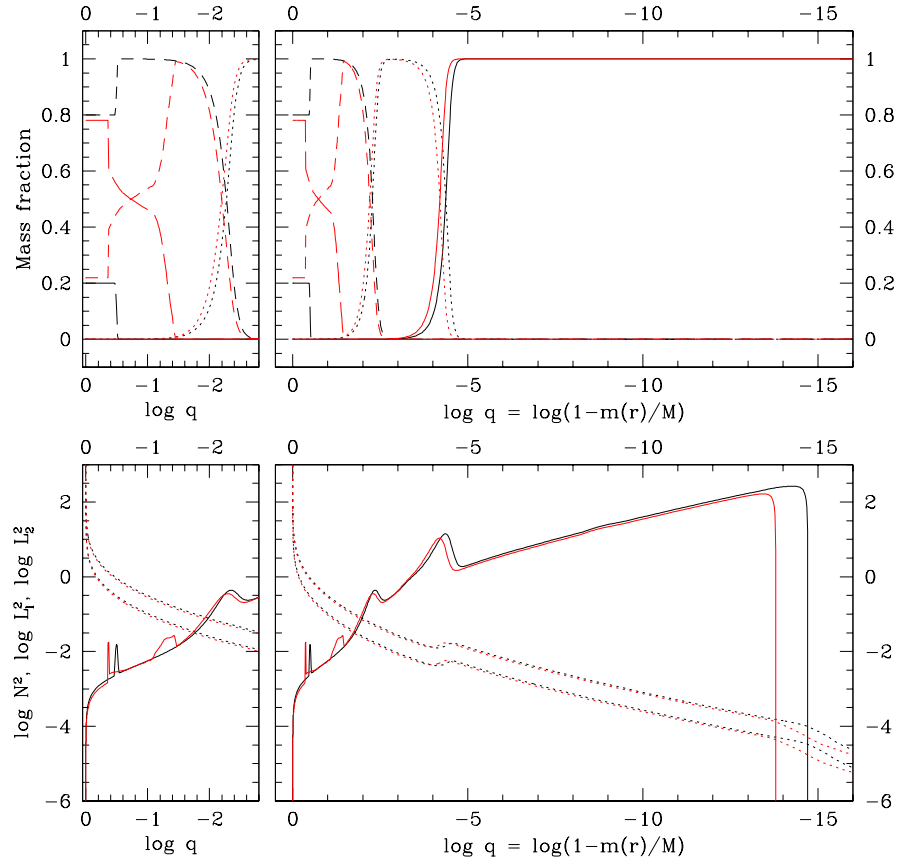


Figure 17

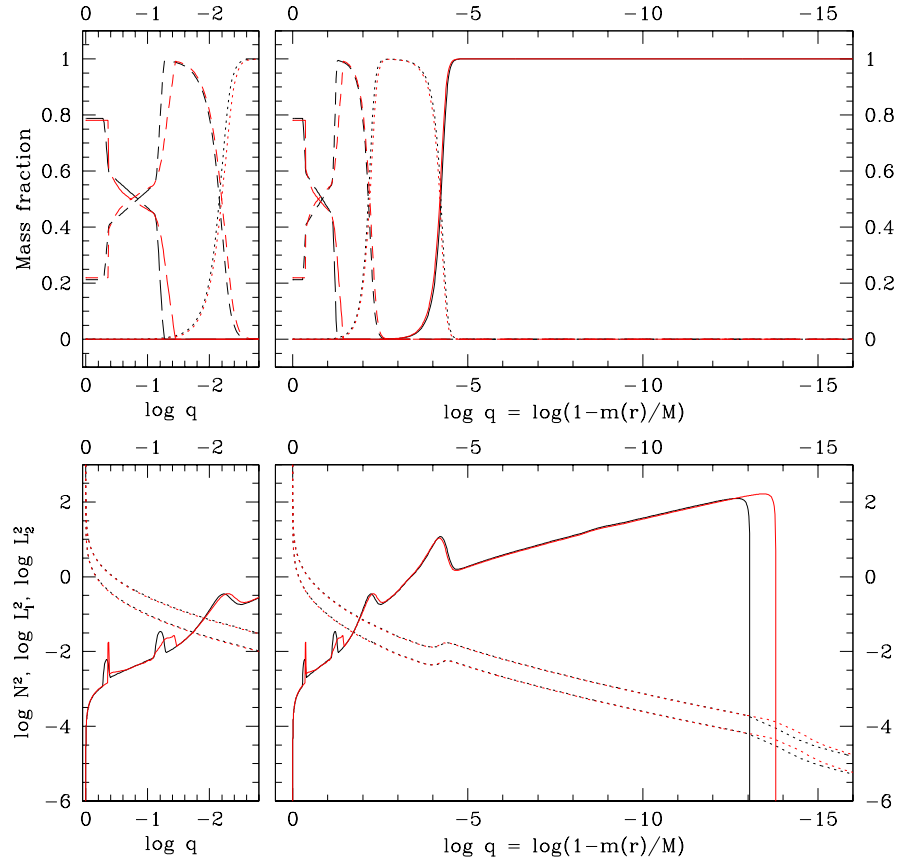


Figure 18